

TOPICAL REVIEW • OPEN ACCESS

Plasmonic titanium nitride nanomaterials prepared by physical vapor deposition methods

To cite this article: Luca Mascaretti *et al* 2023 *Nanotechnology* **34** 502003

View the [article online](#) for updates and enhancements.

You may also like

- [Large scale characterization and calibration strategy of a SiPM-based camera for gamma-ray astronomy](#)
C. Alispach, J. Borkowski, F.R. Cadoux et al.
- [Comment on 'Preparation and antibacterial activity of Fe₃O₄@Ag nanoparticles'](#)
Libor Kvítek and Jana Soukupova
- [Site environment characterization for Southern Wide-field Gamma-ray Observatory](#)
Vlastimil Jílek, Alena Bakalová, Ladislav Chytka et al.

Topical Review

Plasmonic titanium nitride nanomaterials prepared by physical vapor deposition methods

Luca Mascaretti¹ , Cristina Mancarella² , Morteza Afshar^{1,3},
Štěpán Kment^{1,4}, Andrea Li Bassi^{2,5}  and Alberto Naldoni^{1,6}

¹ Czech Advanced Technology and Research Institute, Regional Centre of Advanced Technologies and Materials, Palacký University Olomouc, Šlechtitelů 27, 77900 Olomouc, Czech Republic

² Micro- and Nanostructured Materials Laboratory, Department of Energy, Politecnico di Milano, Via Ponzio 34/3, I-20133 Milano, Italy

³ Department of Physical Chemistry, Faculty of Science, Palacký University, 17. listopadu 1192/12, 77900 Olomouc, Czech Republic

⁴ CEET, Nanotechnology Centre, VŠB-Technical University of Ostrava, 17. listopadu 2172/15, Ostrava-Poruba 708 00, Czech Republic

⁵ Center for Nanoscience and Technology—IIT@PoliMi, Via Rubattino 81, I-20134 Milano, Italy

⁶ Department of Chemistry and NIS Centre, University of Turin, Turin I-10125, Italy

E-mail: luca.mascaretti@upol.cz

Received 4 April 2023, revised 5 June 2023

Accepted for publication 22 September 2023

Published 11 October 2023



CrossMark

Abstract

Titanium nitride (TiN) has recently emerged as an alternative to coinage metals to enable the development of integrated plasmonic devices at visible and medium-infrared wavelengths. In this regard, its optical performance can be conveniently tuned by tailoring the process parameters of physical vapor deposition methods, such as magnetron sputtering and pulsed laser deposition (PLD). This review first introduces the fundamental features of TiN and a description on its optical properties, including insights on the main experimental techniques to measure them. Afterwards, magnetron sputtering and PLD are selected as fabrication techniques for TiN nanomaterials. The fundamental mechanistic aspects of both techniques are discussed in parallel with selected case studies from the recent literature, which elucidate the critical advantages of such techniques to engineer the nanostructure and the plasmonic performance of TiN.


Keywords: titanium nitride, plasmonics, magnetron sputtering, pulsed laser deposition, optical performance

(Some figures may appear in colour only in the online journal)

1. Introduction

Transition metal nitrides (TMNs) are compounds of transition metals of groups 4–6 of the periodic table of elements that, in

general, exhibit valuable properties in terms of technological applications, such as high hardness, high melting point and chemical stability in harsh environments and complementary metal oxide semiconductor (CMOS) compatibility [1]. Among the nitrides of elements of group 4, titanium nitride (TiN) is the most widely used material thanks to the high abundance of Ti on the Earth's crust. TiN can be employed, for example, to produce hard ceramic coatings for industrial

 Original content from this work may be used under the terms of the [Creative Commons Attribution 4.0 licence](https://creativecommons.org/licenses/by/4.0/). Any further distribution of this work must maintain attribution to the author(s) and the title of the work, journal citation and DOI.

parts subject to high wear and harsh environments [2, 3] or for medical devices thanks to its non-toxic nature [4, 5]. Moreover, TiN exhibits a golden luster, which allows decorative usage as a cheaper option than gold (Au) [6].

TiN has been synthesized since the 70s in form of thick coatings or thin films by physical vapor deposition (PVD) [1] or chemical vapor deposition (CVD) [7] methods, predominantly by magnetron sputtering [8]. Breakthroughs in nanofabrication have broadened the range of available techniques to others, including pulsed laser deposition (PLD) [9, 10], molecular beam epitaxy (MBE) [11], and atomic layer deposition (ALD) [12, 13]. In addition to its well-known mechanical and refractory properties, the additional feature of TiN that has recently reconfirmed the interest in this material is its gold-like optical appearance [14, 15]. In this regard, TiN nanomaterials have been considered as an alternative to Au to allow large-scale development of plasmonics [14, 16]. The latter is a broad field of science that exploits the excitation of free-electron resonances under light illumination to induce various effects, including electric field enhancements, electron transfer and heating [17–19], and nonlinear optical effects [20, 21]. In turn, such effects promise intriguing developments in several applications, including solar energy harvesting [22–25], sensing [26, 27] and telecommunication [28, 29]. However, such breakthroughs are currently hindered by the low scalability of the most popular plasmonic metals, i.e. Au and Ag, due to their high cost and incompatibility with microelectronic industry fabrication [30, 31]. This has prompted extensive research toward alternative plasmonic materials, including heavily doped transparent conductive oxides [32–34], non-stoichiometric oxides [35, 36], alkali-noble intermetallics [37, 38], and the already mentioned TMNs [14–16, 39, 40]. In particular, the combination of critical features of TMNs, such as optical tunability, ease of fabrication and refractory nature, suggests a considerable potential of this material class in the field of plasmonics [41, 42]. This, in turn, motivates further investigations and more thorough understanding of the optical and plasmonic properties of TiN, as an archetypal Earth-abundant TMN, in nanostructured form.

In this review, we first introduce the general properties of TiN and present the fundamental optical quantities (complex refractive index and complex permittivity) leading to its characteristic optical and plasmonic behavior. In this regard, a concise overview of the characterization methods to retrieve the complex permittivity of TiN and its theoretical modelling in terms of the Drude–Lorentz model is also included. Afterwards, significant studies addressing the investigation of plasmonic properties of TiN nanomaterials are presented according to the deposition technique. In particular, two PVD techniques have been chosen thanks to their peculiarities and because they have been mostly investigated in terms of optimizing the optical properties of TiN. Conversely, CVD is not considered here because of its main usage to obtain hard coatings [7], while ALD is affected by a slow deposition method and is impractical for films thicker than ~ 100 nm [12, 13]. On the one hand, magnetron sputtering is considered because it is the most widely used method and the most promising in terms of scalability. Furthermore, this technique has recently allowed the

realization of ultrathin TiN epitaxial films exhibiting unprecedented optical properties. On the other hand, PLD is discussed thanks to the possibility of realizing nanostructured films with tunable morphology (including nanoporous films) without the need of substrate patterning nor heating. Finally, we discuss the critical advantages and drawbacks of these technologies in light of further developing the use of plasmonic TiN nanomaterials for light-harvesting applications, especially in terms of solar-energy conversion.

2. General properties of TiN

Titanium nitride (TiN) is a ceramic material that has an extremely rare natural occurrence. Its mineral form indeed, called osbornite, has only been found in meteorites (such as the Bustee meteorite, fallen in 1852 in India) [43]. Nevertheless, this material in synthetic form offers an exceptional combination of refractory and metallic properties that led to a wide range of applications. The reasons for that can be related to the chemical bond between its constituent atoms, i.e. titanium (Ti), with electron configuration $[\text{Ar}]3d^24s^2$, and nitrogen (N), $[\text{He}]2s^22p^3$ (figure 1). In particular, the overall bonding in TiN results from the superposition of an ionic contribution, i.e. electron transfer from a Ti $3d$ orbital to a N $2p$ one, a covalent contribution, i.e. mainly Ti $3d$ –N $2p$ hybridization as well as weak Ti–Ti bond, and a metallic contribution, i.e. due to the d electrons not involved in Ti–N bonds (figures 1(a)–(c)) [44]. As a result, the electronic density of states (DOS) is non-zero at the Fermi level (E_F) [45], which is a typical feature of metals. Such a complex bonding structure provides TiN with both metallic features, such as excellent electrical and optical properties (see section 3), as well as ceramic ones, such as high mechanical and chemical stability, refractory nature (melting point ~ 3000 °C), and excellent hardness [44].

TiN crystallizes in a face-centered cubic (FCC) NaCl crystal structure, usually termed B1-TiN or δ -TiN, with $Fm\bar{3}m$ space group and lattice parameter $a = 4.24$ Å (figure 1(d)) [1, 44]. TiN is actually a non-stoichiometric compound: its B1 cubic structure is stable over a wide range of compositions TiN_x , with $0.6 < x < 1.2$ (figure 1(e)) [45]. In this range, structural stresses and/or point defects, such as N vacancies for under-stoichiometric TiN_x ($x < 1$) or Ti vacancies for over-stoichiometric TiN_x ($x > 1$), can be formed depending on the synthesis conditions [46, 47]. As a result, a variation of the lattice parameter from the reference value is typically found in TiN thin films [48]. Moreover, the visual appearance is also affected by stoichiometry: while stoichiometric TiN has a bright golden color, overstoichiometric films are reddish-brown, while understoichiometric ones are greyish [1]. Such a high tunability of the optical properties of TiN is indeed critical for its applications as plasmonic material (see section 3 for more details). By further varying the nitrogen content outside the stability interval of the B1 phase, other titanium nitrides can be obtained [49]. Theoretical calculations predicted that, by increasing the amount of nitrogen, more Ti–N bonds would form at the expense of Ti–Ti bonds,

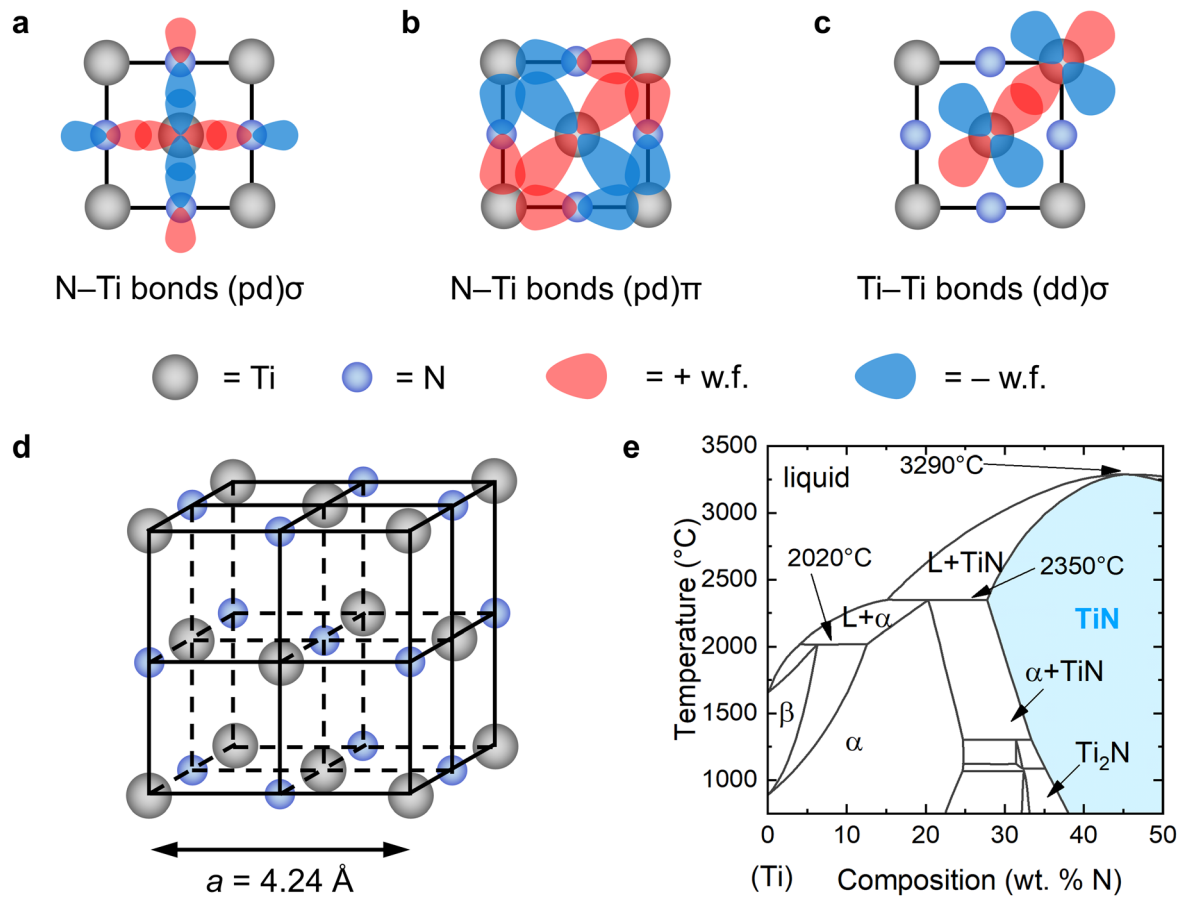


Figure 1. General properties of TiN. (a)–(c) Schematic bonding orbitals in the (100) plane (+w.f. = positive wave function; –w.f. = negative wave function). Reproduced with permission from [45]. Copyright 1986, American Institute of Physics. (d) B1 cubic crystal structure of stoichiometric TiN. (e) Portion of the Ti–N phase diagram, where the light blue shaded area highlights the wide range of stability of the B1 phase TiN_x . Reproduced with permission from [49]. Copyright 2013, Springer Nature.

decreasing the metallicity while increasing the hardness [50, 51]. On the other hand, few of the other phases have been experimentally studied. For example, Ti_2N is a metallic compound that at room temperature and pressure exhibits a tetragonal structure ($\epsilon\text{-Ti}_2\text{N}$) with $P4_2/mnm$ space group [52], but it is not a good optical conductor [53]. On the other hand, metallic titanium pernitride (TiN_2), characterized by a tetragonal $I4/mcm$ crystal structure, has been recently synthesized by high-pressure techniques [54]. Nevertheless, such compounds have all by far a lower importance than TiN from the application point of view.

While TiN has been traditionally applied in hard coatings for cutting tools and machining equipment, it has gained importance also in the microelectronic industry as a diffusion barrier layer in the CMOS technology. In modern integrated circuits, to block the interconnection or diffusion of metal atoms into the Si or SiO_2 substrate, a barrier layer with high conductivity, good adhesion to both the substrate and metals, high-temperature stability, and high mechanical durability is needed. TiN is therefore appropriate in this regard as it exhibits all of these features [55, 56]. More recently, TiN has also been considered as a potential alternative plasmonic material to substitute conventional coinage metals, such as Au, Ag, and Cu. This is because the latter have a high cost, low melting

point, poor chemical stability, low mechanical durability, limited tunability of optical properties, and high carrier concentration resulting in high losses. All of these limitations make them unsuitable for high-temperature applications, optical metamaterials and transformation optics [14, 57]. On the other hand, the aforementioned properties of TiN together with its low-cost, tunable plasmonic resonance in the visible–near-infrared (NIR) range, and limited variation of conductivity and permittivity with temperature make it a valuable alternative material for plasmonic applications [57, 58].

3. Fundamentals of optics and plasmonics

The optical properties of materials are usually investigated by two standard techniques: transmission and reflection spectroscopy, and spectroscopic ellipsometry. The former measures the intensity ratio between transmitted (transmittance, T) or reflected (reflectance, R) light beams upon interaction with a sample compared to a reference light beam. The fraction of light absorbed by the material is termed absorbance and evaluated as [59]

$$A = 1 - (T + R). \quad (1)$$

Usually such measurements are performed at (nearly)-zero angle of incidence. On the other hand, ellipsometry measures the change in polarization of a light beam reflected from a sample [60]. In particular, a linearly-polarized light beam with angle of incidence φ becomes elliptically polarized upon interaction with the sample. The so-called ellipsometric angles Ψ and Δ can be measured, which are related to the Fresnel reflection coefficients in the parallel (r_p) and perpendicular (r_s) direction with respect to the sample surface according to the fundamental equation of ellipsometry:

$$\rho \equiv \tan \Psi e^{i\Delta} = \frac{r_p}{r_s}. \quad (2)$$

Standard reflectance experiments are instead performed with unpolarized light, so that

$$R = \frac{1}{2}(|r_p|^2 + |r_s|^2). \quad (3)$$

The aim of both transmission and reflectance spectroscopy and spectroscopic ellipsometry is to find a quantitative description of the material's complex refractive index or, alternatively, complex dielectric function (or permittivity) [61]. The former is given by

$$\tilde{n}(\omega) \equiv n(\omega) - ik(\omega), \quad (4)$$

where $n(\omega)$ is the (real) refractive index and $k(\omega)$ the extinction coefficient, both of which depending on the angular frequency of the electromagnetic waves ω (the minus sign is used here based on the ellipsometric convention [62]). The complex refractive index has an intuitive physical meaning because $n(\omega)$ and $k(\omega)$ express respectively the refraction and the attenuation of light travelling through a medium. The complex dielectric function has an equivalent physical meaning, and it is given by

$$\tilde{\epsilon}(\omega) \equiv \tilde{n}(\omega)^2 \equiv \epsilon_1(\omega) - i\epsilon_2(\omega). \quad (5)$$

The real and imaginary parts of the dielectric function and of the complex refractive index are mutually related by the following equations [63]:

$$\epsilon_1(\omega) = n^2 - k^2 \quad (6)$$

$$\epsilon_2(\omega) = 2nk \quad (7)$$

$$n = \sqrt{(\epsilon_1 + \sqrt{\epsilon_1^2 + \epsilon_2^2})/2} \quad (8)$$

$$k = \sqrt{(-\epsilon_1 + \sqrt{\epsilon_1^2 + \epsilon_2^2})/2}. \quad (9)$$

The refractive index and the extinction coefficient, in principle, can be directly retrieved from transmission and reflection experiments. The reflectance at normal incidence (considering air as the surrounding medium) in terms of $n(\omega)$ and $k(\omega)$ is simply given by [63]

$$R = \frac{(n(\omega) - 1) + k(\omega)^2}{(n(\omega) + 1) + k(\omega)^2}. \quad (10)$$

However, the same does not hold for the opposite case, i.e. for $n(\omega)$ and $k(\omega)$ as a function of T and R , which require numerical inversion [64]. Additionally, reflectance experiments cannot be done at normal incidence due to instrumental limitations, but with a small angle of incidence ($<10^\circ$), which

also introduces an inaccuracy. On the other hand, if the material of interest presents an uncoated and flat surface, the measured ellipsometric angles can be directly inverted to give the complex dielectric function or the complex refractive index [60]:

$$\langle \tilde{\epsilon}(\omega) \rangle = \langle \tilde{n}(\omega) \rangle^2 = \sin^2 \phi \left[1 + \tan^2 \phi \left(\frac{1 - \rho(\omega)}{1 + \rho(\omega)} \right) \right], \quad (11)$$

where φ is the angle of incidence and ρ is given by equation (2). The use of angle brackets and of the term 'pseudo' here is because the complex dielectric function obtained by direct inversion could be influenced by surface roughness, oxidation or contamination, thus it may differ from the actual one. Nevertheless, in the case of opaque metallic surfaces, the actual complex dielectric function can be reasonably approximated by equation (11). Since most of the literature studies on the optical and plasmonic properties of TiN involve the use of spectroscopic ellipsometry to determine the complex dielectric function [65], in the following we will accordingly present the discussion in terms of $\tilde{\epsilon}(\omega)$ rather than in terms of $\tilde{n}(\omega)$.

Once the dielectric function is experimentally measured, the next step is to find its analytical expression accounting for the electronic properties of the material. In this regard, the classical theory of absorption and dispersion by Lorentz and Drude is sufficiently accurate. In particular, the Lorentz model describes the motion of electrons bound to the nucleus as mechanical harmonic oscillators; in quantum mechanical terms, it represents all the direct interband transitions, and it approximates the behavior of insulators. The Lorentz model can be written as

$$\tilde{\epsilon}(\omega) = 1 + \frac{e^2 N_e}{\epsilon_0 m_e^*} \frac{1}{\omega_0^2 - \omega^2 + i\gamma\omega}, \quad (12)$$

where e is the elementary charge, N_e is the number density of electrons, ϵ_0 is the vacuum permittivity, m_e^* is the electron effective mass, ω_0 is the resonance frequency of oscillation, and γ is the damping factor. On the other hand, the Drude model describes the motion of electrons with damping but without restoring force; in quantum mechanical terms, it represents the intraband transitions, i.e. the optical absorption by free electrons in metals [63]. The Drude equation can be obtained by the Lorentz oscillator setting $\omega_0 = 0$, i.e.

$$\tilde{\epsilon}(\omega) = 1 - \frac{e^2 N_e}{\epsilon_0 m_e^*} \frac{1}{\omega^2 - i\gamma\omega} = 1 - \frac{\omega_p^2}{\omega^2 - i\gamma\omega} \quad (13)$$

where the term

$$\omega_p = \sqrt{\frac{N_e e^2}{\epsilon_0 m_e^*}} \quad (14)$$

is defined as the unscreened plasma frequency. These two models can be combined together to describe the behavior of real conductor materials, including noble metals (such as Au and Ag) and intermetallic compounds (such as TiN). A typical expression for a combined Drude–Lorentz model used

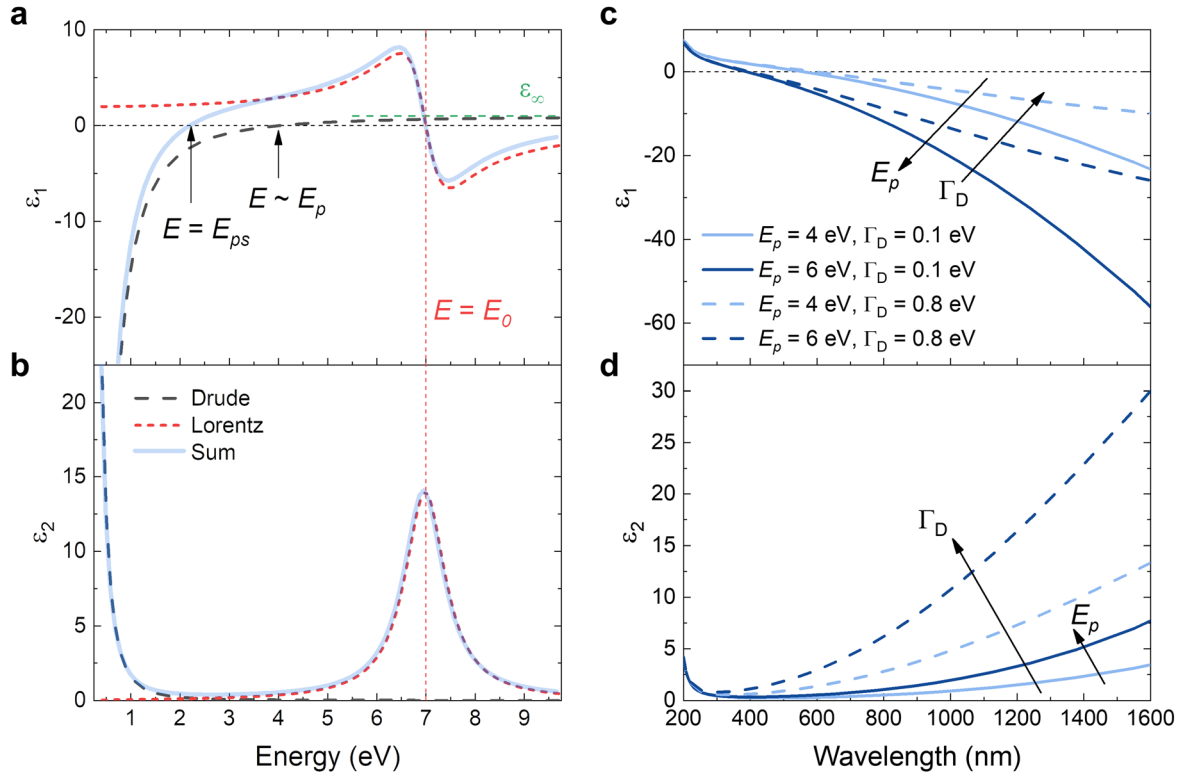


Figure 2. Dielectric function of a hypothetical conductor material modeled by one Drude and one Lorentz oscillators ($\epsilon_\infty = 1$, $E_p = 4$ eV, $\Gamma_D = 0.1$ eV, $f_1 = 2$, $E_{0,1} = 7$ eV, $\Gamma_{L,1} = 1$ eV, with the meaning of the parameters according to equation (15)). (a) Real and (b) imaginary parts represented as a function of energy (in eV). (c) Real and (d) imaginary parts represented as a function of the wavelength (in nm), in which the effect of changing either the unscreened plasma energy or the damping factor is illustrated.

in the ellipsometric community in energy units (eV) instead of in angular frequency units (in cm^{-1}) is given by [66]

$$\tilde{\epsilon}_{D-L}(E) = \epsilon_\infty - \frac{A_D}{E^2 - i\Gamma_D E} + \sum_j \frac{f_j E_{0,j}^2}{E_{0,j}^2 - E^2 + i\Gamma_{L,j} E}. \quad (15)$$

In equation (15) the first term (ϵ_∞) is a high-frequency constant accounting for the polarization of bound electrons in the d electronic band. The second term is the Drude oscillator where the parameters are the amplitude A_D , which is the square of the unscreened plasma energy, $A_D = E_p^2 = (\hbar\omega_p)^2$, and the damping factor $\Gamma_D = \hbar\gamma_D = \hbar/\tau_D$, where τ_D is the relaxation time (fs). The third term is a sum of Lorentz oscillators, each one with a strength f_j (non-dimensional in this formulation), center energy $E_{0,j} = \hbar\omega_{0,j}$ and damping factor $\Gamma_{L,j} = \hbar\gamma_{L,j}$.

Figure 2 illustrates a hypothetical conductor material whose complex dielectric function is modeled by the sum of a Drude oscillator and a single Lorentz oscillator. In the low-energy region, the conductor behaves essentially as an ideal Drude metal, so that $\epsilon_1 < 0$ (figure 2(a)) and ϵ_2 shows a maximum (figure 2(b)). In this region, light is partially absorbed by intraband transitions, i.e. electronic transitions from occupied states to unoccupied states within the same band, and the rest is reflected. By increasing the energy, ϵ_1 crosses the x axis (figure 2(a)) while ϵ_2 is nearly zero (figure 2(b)). The condition $\epsilon_1 = 0$ defines a resonant frequency for the propagation of collective longitudinal (LO)

oscillations of electrons, i.e. the so-called volume plasmon [61, 63]. For an ideal Drude metal, this point corresponds to the unscreened plasma frequency ω_p (or energy, E_p , dashed line in figure 2(a)). For a real conductor, the contribution of the interband transitions (in this case represented by the Lorentz oscillator) shifts this transition to a lower energy value, called screened plasma energy (E_{ps}), or also crossover wavelength (λ_{ps}). Therefore, for $E > E_{ps}$ (or $\lambda < \lambda_{ps}$), ϵ_1 becomes positive and light is partially transmitted through the material. By increasing the energy, ϵ_2 increases reaching a second maximum at $E = E_{0,1}$, i.e. the center energy of the Lorentz oscillator (figure 2(b)). In this region, strong light absorption occurs by interband transitions, i.e. electronic excitations occurring between two different bands. Finally, for $E > E_{0,1}$, ϵ_1 becomes once again negative (figure 2(a)) and ϵ_2 decreases (figure 2(b)), which corresponds to another region of light reflection.

An equivalent way of illustrating the complex dielectric function is as a function of wavelength, as shown in figures 2(c) and (d). In particular, those panels illustrate the effect of changing the Drude parameters (E_p and Γ_D), while keeping constant the Lorentz oscillator, on the ϵ_1 (figure 2(c)) and ϵ_2 (figure 2(d)) spectra. It is possible to observe that an increase in E_p (i.e. in the metallic character of the conductor) produces a decrease in ϵ_1 and a moderate increase in ϵ_2 . On the other hand, an increase in Γ_D (i.e. in the dissipative character of the conductor) produces an increase in ϵ_1 and a substantial increase in ϵ_2 . Therefore, an ideal metallic material

would exhibit very low (negative) values of ε_1 as well as relatively low values of ε_2 .

The volume plasmons defined above are rarely observed and two other kinds of plasmons can be defined, which are typical of nanostructured materials [67]. The first ones are surface plasmon polaritons (SPPs), which consist in travelling electromagnetic waves along the interface between a dielectric and a conductor and are evanescently confined in the perpendicular direction; the characteristic frequency is given by

$$\omega_{\text{SPP}} = \frac{\omega_p}{\sqrt{1 + \varepsilon_m}} \quad (16)$$

in which it is assumed that the insulator has a real dielectric constant (such as air, $\varepsilon_m = 1$). The second ones are localized surface plasmons (LSPs), which consist in non-propagating oscillations of conduction electrons in nanostructures such as nanoparticles, nanorods, etc. In the quasi-static approximation, which considers a spherical nanoparticle of radius R_{NP} much smaller than the incident wavelength ($R_{\text{NP}} \ll \lambda$), the localized surface plasmon resonance (LSPR) frequency is given by the formula

$$\omega_{\text{LSPR}} = \sqrt{\frac{\omega_p^2}{\varepsilon_\infty + 2\varepsilon_m} - \Gamma_D} \simeq \frac{\omega_p}{\sqrt{1 + 2\varepsilon_m}}, \quad (17)$$

where the approximation is made for a purely Drude metal (which is the typically reported formula). Knowledge on the complex dielectric function of the material and its unscreened plasma frequency, thus, allows predicting the conditions for the SPPs and LSPR. For the latter case, the expression of $\tilde{\varepsilon}(\omega)$ should be modified to take into account the nm-sized dimension of the nanoparticle [68].

The complex dielectric function can provide additional information on the plasmonic properties of the materials by computing the so-called plasmonic quality factors for SPPs and for the LSPR [69], respectively

$$Q_{\text{SPP}} = \varepsilon_1^2 / \varepsilon_2 \quad (18)$$

$$Q_{\text{LSPR}} = -\varepsilon_1 / \varepsilon_2, \quad (19)$$

where the latter is calculated in the quasi-static approximation. The so-called maximum values for the plasmonic quality factors can further be computed in the Drude approximation according to the formulas [37]

$$Q_{\text{SPP}}^{\text{max}} = \frac{E_{pu}^2}{2\Gamma_D^2} \quad (20)$$

$$Q_{\text{LSPR}}^{\text{max}} = \frac{2(E_{pu}^2 - \Gamma_D^2 \varepsilon_\infty)^{3/2}}{3\sqrt{3}\varepsilon_\infty \Gamma_D E_{pu}^2}. \quad (21)$$

Still within the simple Drude theory [46], further interesting quantities in terms of the electrical behavior of the material can be computed, such as the mean free path of conduction electrons

$$\text{MFP} = \left[\frac{3\pi^2 \varepsilon_0 \hbar^4}{(em_e^*)^2} \right]^{1/3} \frac{E_{pu}^{2/3}}{\Gamma_D} \quad (22)$$

and the electrical resistivity

$$\rho_{\text{opt}} = \frac{\hbar \Gamma_D}{E_{pu}^2 \varepsilon_0}. \quad (23)$$

In equation (23), the subscript ‘opt’ has the meaning to discern the electrical resistivity calculated with the Drude parameters (obtained, for example, by ellipsometry) from the directly measured one (such as by the Van der Pauw method).

Figure 3 presents an overview on the optical properties of TiN continuous films prepared by either magnetron sputtering or PLD. The wavelength range from ~ 200 to ~ 500 nm is the region of interband absorption, which is associated with positive values of ε_1 (figure 3(a)) and a local maximum in ε_2 (figure 3(b)). The main interband transitions in TiN (figure 3(c)) occur from p orbitals of N atoms, lying around -5.5 eV and -3.5 eV below the Fermi level (E_F), to d orbitals (with t_{2g} symmetry) of Ti atoms above E_F . Such transitions are labeled as E_{01} and E_{02} , respectively, and are usually represented by two Lorentz oscillators in the modeling of the complex dielectric function [65]. On the other hand, the wavelength range >600 nm is the region of intraband absorption, featuring negative and decreasing values of ε_1 (figure 3(a)) and increasing values of ε_2 (figure 3(b)). This means that the interaction of TiN with visible or infrared wavelengths occurs via quasi-free electron oscillations, i.e. as in a Drude-like metal. TiN materials with highly metallic character are thus characterized by low negative values of ε_1 and low positive values of ε_2 (figures 3(c) and (d); see also the discussion below).

The plot of the DOSs in figure 3(c) also shows the hybridization between N $2p$ orbitals and Ti $3d$ orbitals, which gives rise to the chemical bonding in TiN. The Ti $3d$ band crosses E_F with a much higher value compared to the N $2p$ band, meaning that the electronic conductivity in TiN is mostly ascribed to the Ti $3d$ electrons [65]. For this reason, the [Ti]/[N] ratio, i.e. the stoichiometry x in TiN_x materials, has a deep influence on their optical, electrical and plasmonic properties. For example, the ε_1 spectra reported in figure 3(a) show a substantial variation depending on the preparation conditions: not only stoichiometry, but also impurities (especially oxidation) and grain size affect the optical performance of TiN. In particular, it was found [70] that the crossover wavelength λ_{ps} correlates with x , as represented by the colored intervals in the inset of figure 3(a). In particular, a perfectly stoichiometric TiN film exhibited $\lambda_{ps} \sim 470$ nm ($E_{ps} \sim 2.65$ eV); on the other hand, over-stoichiometric films (i.e. TiN_x with $x > 1$) exhibited higher λ_{ps} (lower E_{ps}), while the opposite occurred for under-stoichiometric films (i.e. TiN_x with $x < 1$), i.e. a lower λ_{ps} (higher E_{ps}). The inset of figure 3(a) shows that actual deviations from the ideal 1:1 stoichiometry are common in the reported data for TiN materials prepared by sputtering as well as PLD. The ε_1 and ε_2 data in figures 3(a) and (b) can be employed to calculate the reflectivity at normal incidence by equation (10) (figure 3(d)). The reflectivity of TiN generally features a minimum between ~ 350 and ~ 450 nm, while it goes close to unity ($R \sim 0.9$) in the near-infrared range; as a result, TiN typically exhibits a gold-like color. On the other hand, figures 3(e) and (f) show the plasmonic quality factors for

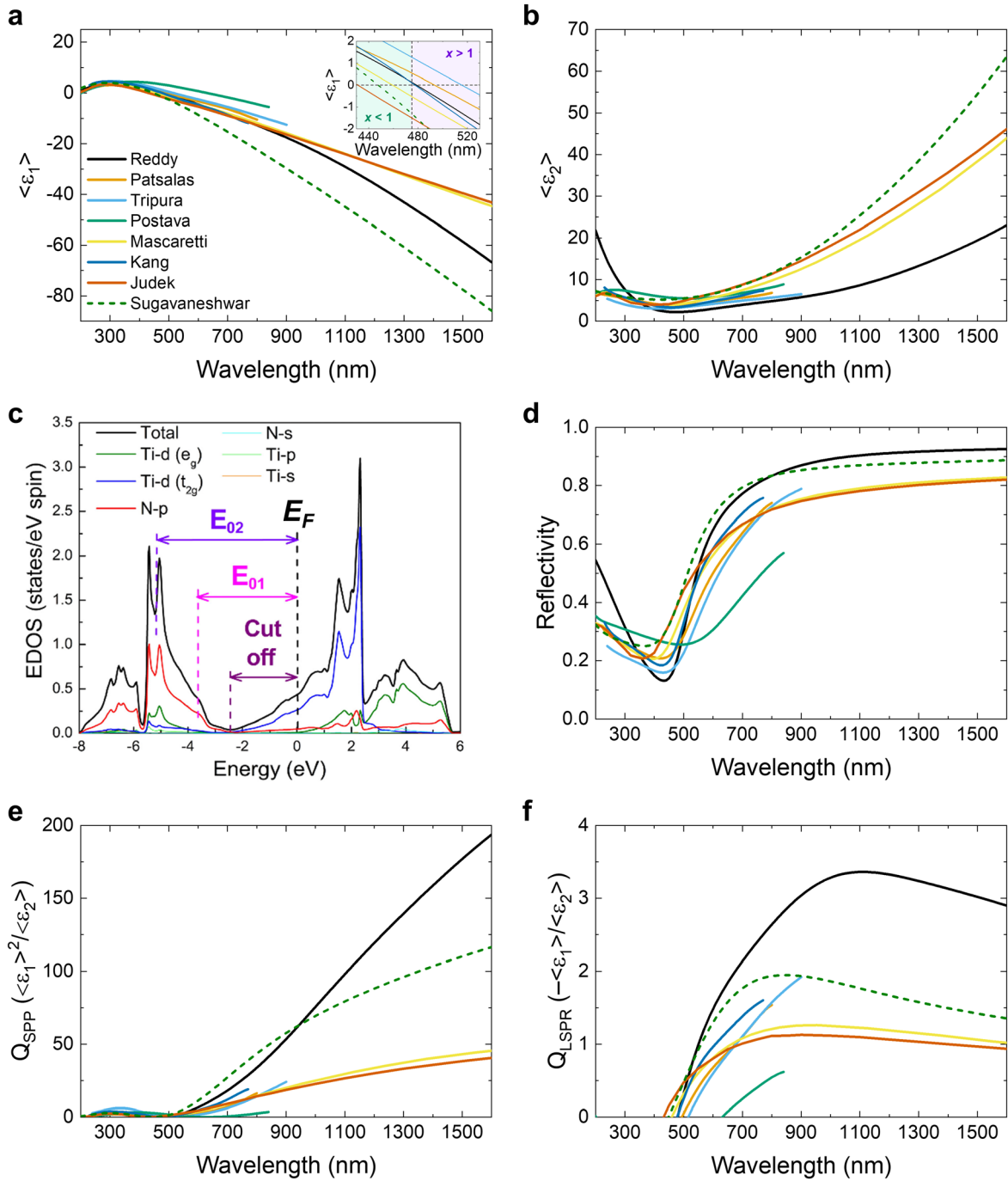


Figure 3. Overview of literature data on the optical properties of TiN thin films deposited by sputtering (solid lines) or PLD (dashed line). (a) Real and (b) imaginary parts of the complex dielectric function measured by spectroscopic ellipsometry; the inset in (a) shows in more detail the crossover wavelength and its correlation with the film stoichiometry (TiN_x). (c) Electron density of states calculated by DFT. Reproduced from [15]. [CC BY 4.0](https://creativecommons.org/licenses/by/4.0/) (d) Reflectivity spectra computed by equation (10) from the data in (a) and (b). (e) Quality factor for surface plasmon polaritons (equation (18)) and (f) for localized surface plasmons (equation (19)) for TiN thin films deposited by sputtering and PLD. For the panels a–b and d–f, the data were taken from Reddy *et al* [71], Patsalas and Logothetidis [46], Tripura Sundari *et al* [74], Postava *et al* [73], Mascaretti *et al* [72], Kang and Kim [70], Judek *et al* [75], and Sugawaneshwar *et al* [9].

SPPs and LSPRs, respectively, calculated by equations (18) and (19). Both Q_{SPP} and Q_{LSPR} have physical meaning in the region where $\epsilon_1 < 0$, i.e. the region of intraband transitions and, thus, of metallic behavior. It is possible to observe a superior behavior for the epitaxial film grown at high temperature on sapphire in both cases ($Q_{\text{SPP}} \sim 184.3$ at the telecommunication wavelength of 1550 nm and $Q_{\text{LSPR}} \sim 3.4$ at

1100 nm) [71], followed by the film deposited by PLD ($Q_{\text{SPP}} \sim 113.1$ at 1550 nm and $Q_{\text{LSPR}} \sim 1.4$ at 1020 nm) [9]. On the other hand, the TiN films prepared by magnetron sputtering exhibit rather similar plasmon performance (for example, $Q_{\text{SPP}} \sim 44.3$ at 1550 nm and $Q_{\text{LSPR}} \sim 1.3$ at 954 nm for the film reported in [72]), apart from that reported in [73], which probably exhibited a substantial over-stoichiometry.

4. TiN by magnetron sputtering

4.1. Fundamentals of magnetron sputtering

Magnetron sputtering is a widely used PVD method employed both in research and in industry for thin films and coatings deposition. This method is based on the phenomenon of sputtering, which consists in the vaporization of the surface of a target material by energetic ions that penetrate the target causing collision cascades. Ions can be provided by a glow discharge resulting from the ionization of a gas at low pressure (~ 10 Pa) by application of a potential difference between a cathode (the target) and an anode enclosed within a vacuum chamber (figure 4(a)). Energetic ions colliding against the target give rise not only to the ejection of target atoms, but also to secondary electrons, which sustain the discharge because they are accelerated from the cathode to the anode and ionize the gas, which in turn bombard the cathode, releasing further secondary electrons and sputtered atoms [76]. The sputtering yield, $Y(E_i)$, is defined as the ratio between the number of sputtered atoms and that of incident ions and can be simply approximated by the empirical formula [77]

$$Y(E_i) = aE_i^b, \quad (24)$$

where E_i is the kinetic energy of the incoming ions (\sim hundreds of eV), while a and b are fit parameters that depend on the ion and target species. The sputtered atoms have typically a kinetic energy of \sim few eV and travel through the plasma in few μ s, thus with a little chance of ionization. Therefore, most of the sputtered species are neutral atoms, while small fractions of ionized atoms and cluster of atoms are also obtained. The operating pressure in the chamber must be an optimum to allow ionization events by secondary electrons and to prevent scattering events among sputtered species and gas atoms. The sputtered species can be therefore collected on a substrate, giving rise to film deposition. This means that the mean free path of the sputtered atoms must be higher than the target-substrate distance (d_{T-S} in figure 4(a)). On the other hand, the sputtered species in the vicinity of the target can also be ionized by secondary electron and be attracted back toward the target, participating to the sputtering process. This phenomenon is called self-sputtering [76].

The first sputtering deposition devices were based on a glow discharge provided by a direct current (DC). The use of a magnetron was then proposed, which consists of a magnet that traps the electrons in the proximity of the target (kept at a constant negative voltage), thus increasing their lifetime and lowering the operative pressure to ~ 1 Pa (figure 4(b)). The sputtering process in this configuration is therefore termed direct current magnetron sputtering (DCMS, figure 4(c)) and is ideal for depositing thin metallic films. On the other hand, the voltage applied to the target can be varied with high frequencies (such as 13.56 MHz) to allow depositing insulators, which is termed radiofrequency magnetron sputtering [78]. Furthermore, the deposition rate and the ionization degree of the plasma (which benefits the film quality) can be increased by increasing the plasma density, which in turn increases by increasing the power density supplied to the

target. However, the latter is limited by the target damage threshold (~ 0.05 kW cm $^{-2}$). Therefore, higher peak power densities can be achieved by reducing the duty cycle (i.e. the time fraction of one period in which the system is active), and this method is termed high power pulsed magnetron sputtering (HPPMS, figure 4(c)) [76]. A particular case is that of high power impulse magnetron sputtering (HiPIMS, figure 4(c)), in which case the peak power exceeds the time-averaged power by two orders of magnitude [77]. In HiPIMS, peak power densities up to ~ 10 kW cm $^{-2}$ and duty cycles as low as 0.5% can be achieved and it offers a wide spectrum of potential advantages compared to DCMS, including, for example, improved adhesion [79], higher film density [80], and lower electrical resistivity [81]. An intermediate situation between DCMS and HiPIMS is the modulated pulse power approach (MPP, figure 4(c)), which consists in keeping a moderate power level for the first part of the pulse followed by a high power pulse [82].

Regardless the specific method, sputter deposition can be applied to deposit compound films or coatings either by directly sputtering the desired compound target (i.e. TiN) or by sputtering an elemental target (i.e. Ti) in a gas mixture of an inert working gas (i.e. Ar) and a reactive gas (i.e. N $_2$). The latter process is termed reactive sputtering and allows, for example, preparing a wide range of compounds, typically oxides and nitrides, from low-cost metal targets and tuning their functional properties by controlling the deposition parameters. The reactive gases in the chamber, however, also react with the surface atoms of the target, which affects the sputtering yield and the yield of secondary electron. If a compound layer is formed at the target surface (i.e. an oxide layer on a metallic target), this effect is called ‘poisoning’ [76, 77]. Nevertheless, sputtering deposition presents also some drawbacks. For example, it usually produces a ‘shadowing’ effect when depositing on surfaces characterized by small features, contrarily to ALD, which leads to high conformality of the growing film. Moreover, the as-grown films often suffer from residual stresses related to lattice mismatch with the substrate, which can be limited by employing substrates favoring epitaxial growth, such as (001)MgO or (0001)Al $_2$ O $_3$. Additionally, the tunability on the morphology of the films produced by sputtering is also limited in terms of forming nanoporous structures, which can be addressed by employing PLD, as discussed in section 5.

4.2. Optimization of TiN resistivity and plasmonic properties

The properties of TiN thin films prepared by magnetron sputtering have been extensively investigated in the literature. Studies around the end of 90’s and beginning of 2000s, for example, described the change of the structural and optical properties of TiN by varying the substrate bias voltage (V_b) or temperature [46, 70, 84]. The optical properties have been largely monitored by spectroscopic ellipsometry to retrieve the complex refractive index (section 3). An important aspect is the optical behavior of TiN $_x$ materials with respect to the stoichiometry (see also section 2). In particular, Kang and Kim investigated the stoichiometry of TiN $_x$ films prepared by

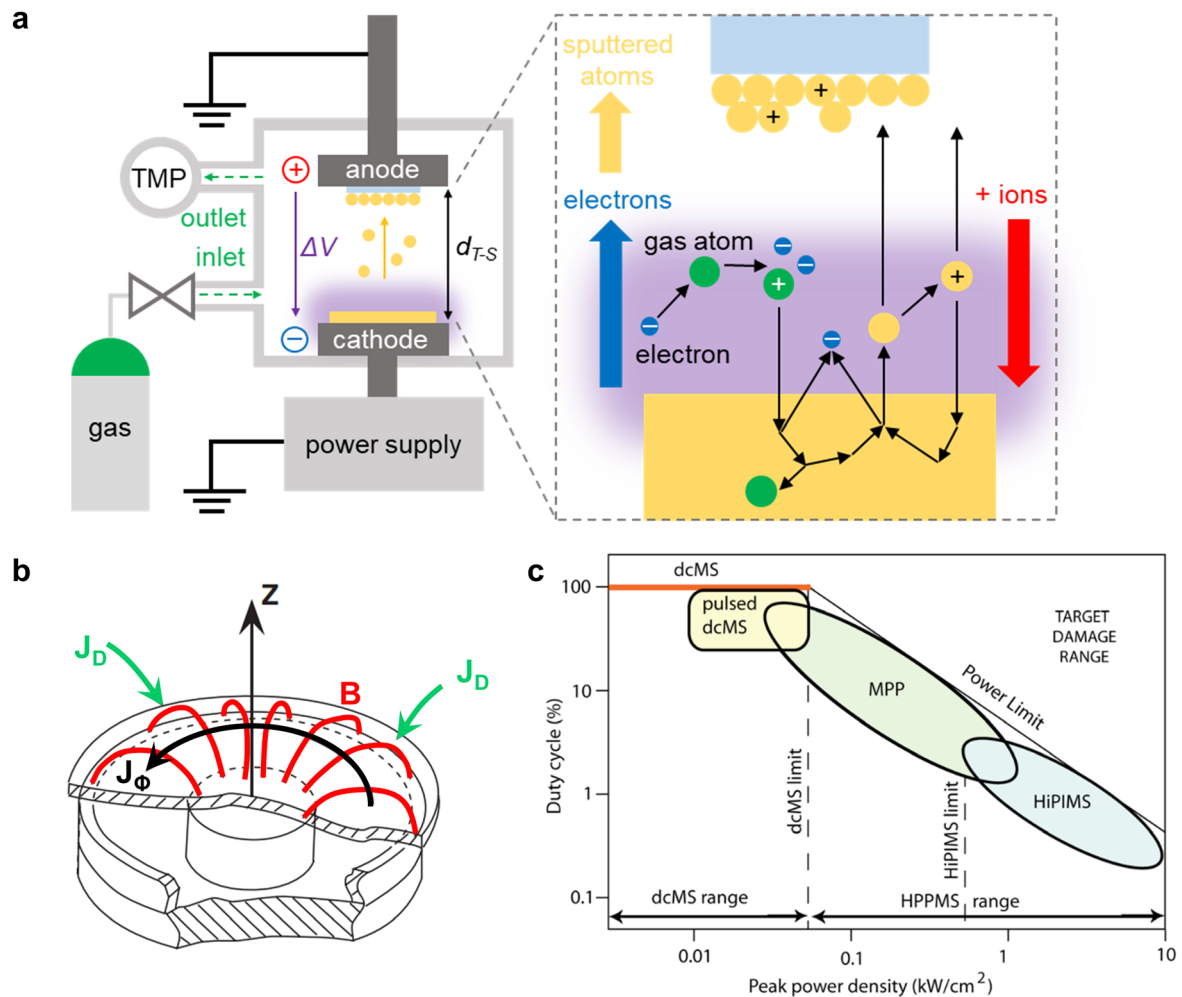


Figure 4. General features of magnetron sputtering. (a) Schematic of a typical experimental setup consisting of a vacuum chamber, which contains the target (cathode), connected to a power supply and the substrate (anode) separated by a target-to-substrate distance d_{T-S} . The application of a potential difference between the anode and the cathode triggers a collision cascade in the latter by means of energetic ions in the gas, ultimately leading to film deposition on the substrate. (b) Schematic of the planar magnetron magnet assembly and the cathode target, where the magnetic field lines B are radial, while J_{ϕ} and J_D represent the azimuthal and discharge current densities, respectively. Adapted with permission from [83]. Copyright 2009, American Institute of Physics. (c) Nomenclature for pulsed discharges based on the peak power density at the target combined with the duty cycle. Reproduced with permission from [76]. Copyright 2012, American Vacuum Society.

reactive DCMS from a Ti target by varying the N_2 flow rate (1.5–4.5 sccm) [70]. The film composition was determined by XPS analysis, which further revealed a linear relationship between the lattice constant (retrieved by XRD) and the nitride composition in the range $0.7 < x < 1.2$. Furthermore, by extracting the complex refractive index from ellipsometric measurements, a redshift of the crossover wavelength (λ_{ps}) or decrease of the screened plasma energy (E_{ps}) was found, where a perfectly stoichiometric TiN film was associated to $\lambda_{ps} \sim 470$ nm and $E_{ps} \sim 2.65$ eV, respectively (figure 5(a)). By fitting the intraband region with a Drude model, a maximum in the carrier relaxation time (τ_D) around $x = 1$ was found, which corresponded to a minimum in both the optical (equation (23)) and the experimentally-measured resistivity. A similar analysis has further been reported more recently by Judek *et al* [75], who also controlled the film stoichiometry by varying the N_2/Ar gas flux during reactive DCMS from a Ti target. However, in this case the film composition was determined by secondary ion mass spectroscopy (SIMS) under ultra-high vacuum calibrating

the signal with a reference stoichiometric TiN. The appearance of the films visibly changed with the composition, with the stoichiometric film exhibiting a golden color, in agreement with the previous literature. The authors further investigated the optical properties of the films by ellipsometry not only in the UV–visible–NIR range, but also in the medium-IR (MIR). By correlating λ_{ps} (or E_{ps}) and the nitride stoichiometry x , the authors found a qualitative agreement with the results of [70], with nearly identical data for the stoichiometric film ($\lambda_{ps} \sim 479$ nm and $E_{ps} \sim 2.59$ eV, figure 5(a)). However, for under- and over-stoichiometric compositions, more pronounced changes in λ_{ps}/E_{ps} values were found in [75] rather than in [70], which could be related to the use of a different technique for determining the atomic composition of the materials. Therefore, while a gold-like color and a crossover wavelength falling in the range 465–480 nm can be fairly associated with stoichiometric TiN, substantially over- or under-stoichiometric TiN_x compositions should be carefully measured by dedicated experiments.

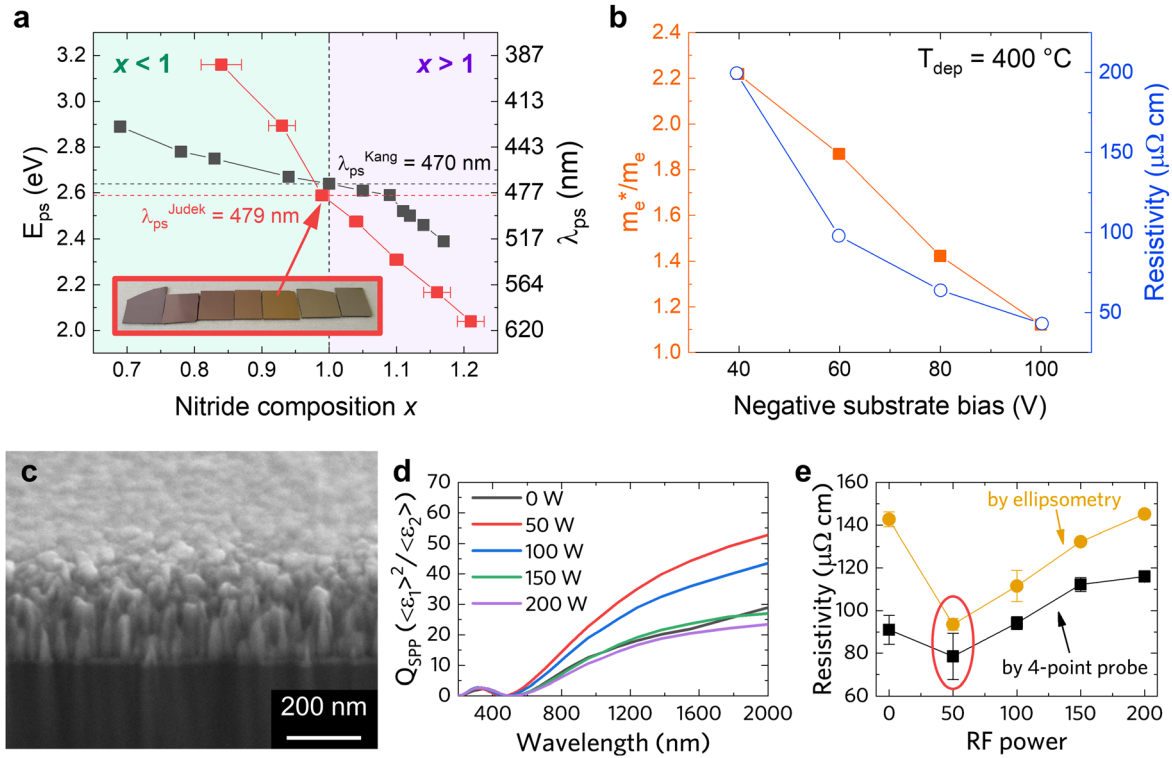


Figure 5. (a) Screened plasma energies calculated by the Drude model (E_{ps}) and crossover wavelengths (λ_{ps}) of TiN_x materials as a function of the composition x , comparing the data from Kang and Kim [70] (black) and from Judek *et al* [75] (red and inset picture). Inset reproduced from [75]. Copyright 2021 Author(s), licensed under a CC-BY Creative Commons Attribution 4.0 License. (b) Variation of the normalized effective mass (m_e^*/m_e) and resistivity of TiN_x thin films with the substrate bias voltage. Reproduced from [84]. Copyright 1999, American Institute of Physics. (c) Representative cross-sectional SEM/FIB image, (d) quality factor for SSPs and (e) electrical resistivity (directly measured by four-point probe technique and retrieved by Drude parameters) of TiN thin films deposited by pulsed DC magnetron sputtering with varying RF substrate biasing. Reproduced from [72]. Copyright 2021, Elsevier.

Patsalas and co-workers further investigated the electrical and mechanical properties of TiN_x thin films by controlling the substrate bias voltage (V_b) and the deposition temperature [84]. In that study, the value of the electron effective mass (m_e^*) was calculated from spectroscopic ellipsometry data via equation (14) and from the density of charge carriers obtained by Hall effect measurements. The authors found a decrease of both the electron effective mass and the resistivity with $|V_b|$ (figure 5(b)). In particular, the ratio m_e^*/m_e approached unity at high $|V_b|$, i.e. $m_e^*/m_e \sim 1.15$ at $V_b = -100$ V, suggesting a closer behaviour to ideal metals [63]. Since such conditions promoted the growth of stoichiometric TiN with optimal electrical conductivity, the value of the effective mass for stoichiometric TiN could be set as $m_e^* \sim 1.15 m_e$ with a fair degree of approximation. Such value can be then employed to estimate the MFP of conduction electrons by equation (22). Building up from the results of that study, Patsalas and co-worker further studied TiN_x thin films deposited by DCMS with the aim of establishing a correlation between the optical and electronic properties with microstructure and process parameters [46]. In particular, the authors showed the possibility of employing the Drude–Lorentz analysis of ellipsometric data to estimate not only the film resistivity (equation (23)), but also its mass density, according to the

simple Drude theory of metals [61], with the formula

$$\rho_m = \frac{\epsilon_0 m_e^* A E_{pu}^2}{(e^2 N_A Z \hbar^2) / 10^6}, \quad (25)$$

where $A = A_{Ti} + A_N = 62$ amu is the atomic mass of the metal, N_A is Avogadro's number, $Z = 0.95$ is the mean number of conduction electrons per TiN molecule, and 10^6 is a unit conversion factor (ρ_m in $g\ cm^{-3}$ using $\hbar = 6.582 \cdot 10^{-16}$ eV·s). In particular, a substrate bias voltage $|V_b| > 100$ V at the substrate temperature $T_d = 400$ °C led to higher density compared to bulk TiN, i.e. $\sim 5.7\ g\ cm^{-3}$ versus $5.21\ g\ cm^{-3}$ [85]. Furthermore, highly metallic and stoichiometric TiN films with a resistivity as low as $40\ \mu\Omega\ cm$ were achieved by sputtering at high substrate bias voltage and temperature ($|V_b| > 100$ V, $T_d = 650$ °C). This was ascribed to two different mechanisms: on the one hand, a higher substrate temperature favoured the grain growth, thus reducing the scattering events at the grain boundaries; on the other hand, an increase in $|V_b|$ induced sputtering of N atoms, thus reducing Ti vacancies and filling microvoids [63].

In this regard, a recent study thoroughly discussed the relationship among structural properties, plasmonic quality factors and electrical resistivity of TiN_x thin films [72]. The materials were prepared by DCMS at room temperature by applying RF substrate biasing in the range 0–200 W with the

aim of inducing an additional self-bias. All the investigated films exhibited a similar morphology irrespectively of the growth conditions, characterized by vertically-oriented columnar structures (figure 5(c)). While the films grown in absence of RF substrate biasing exhibited a preferential growth along the [111] direction, ion bombardment arising from the additional self-bias induced a texturing effect, leading to preferential growth along the [200] and [220] directions. In particular, the ellipsometric analysis revealed that the metallicity of the films could be optimized under moderate substrate biasing (i.e. at the RF power of 50 W), as demonstrated by the enhanced plasmonic quality factors for both SPPs (figure 5(d)) and LSPR. The Drude–Lorentz analysis of the ellipsometric spectra revealed that, in such conditions, several quantities related to the Drude parameters were maximized, including the film stoichiometry ($x = 0.85$, while all the other films were over-stoichiometric, i.e. $x > 1$), the mean free path of conduction electrons (equation (22)), and the electrical resistivity (equation (23)). The latter was then compared to experimental measurements performed by four-point probe (van der Pauw) method, finding a good qualitative agreement (figure 5(e)).

4.3. High-temperature optical performance of epitaxial TiN films

Epitaxial growth on highly crystalline substrates, such as (0001)-oriented Al_2O_3 (heteroepitaxy) [71, 86–88] and MgO (001) [89, 90], has been considered as an efficient strategy to achieve TiN thin films with superior crystalline and optical quality. Such studies have also considered the effect of temperature either during the film growth [86] or during spectroscopic ellipsometry by keeping the sample in vacuum to investigate the evolution of the permittivity [71, 74, 90]. For example, the authors of [71] prepared single-crystalline TiN films on (0001)-oriented Al_2O_3 by DCMS at the temperature of 850 °C and investigated the temperature-dependent optical properties up to 900 °C by an *in situ* optical ellipsometry setup in a high vacuum chamber. The real and the imaginary part of the dielectric function decreased and increased in magnitude with temperature, respectively, which was mostly due to an increase in the Drude broadening Γ_D (see also figures 2(c) and (d)). The latter, in turn, was ascribed to an increase in electron–phonon scattering rate, a change in the electron effective mass and a reduction of the carrier density. In addition, the plasmonic quality factor for SPPs was evaluated as [67, 91]

$$L_{\text{SPP}} = \lambda_0 \frac{\varepsilon_1^2}{2\pi\varepsilon_2} \left(\frac{\varepsilon_1 + \varepsilon_m}{\varepsilon_1\varepsilon_m} \right)^{3/2}, \quad (26)$$

where λ_0 is the free space wavelength, to include the contribution of an adjacent dielectric (with real ε_m). On the other hand, the quality factor for LSPR (Q_{LSPR}) was evaluated according to equation (19). Figures 6(a) and (b) show L_{SPP} and Q_{LSPR} for TiN compared with the same for Au and Ag from room temperature up to 900 °C. Notably, while the plasmonic properties of TiN were inferior to those of noble metals at room temperature, such performance gap almost

vanished at 400 °C. In addition, TiN did not exhibit structural degradation at high temperature regimes, contrarily to Au and Ag [57, 92], thus appearing as a suitable plasmonic material for high-temperature applications. In this regard, the authors performed opto-thermal simulations of heating under optical excitation in a diabolito antenna (DA) array made of Au, Ag and TiN on sapphire substrate. In particular, TiN DAs under 61 mW resonant excitation exhibited a highly uniform temperature ~ 880 °C (figure 6(c)) and a more stable response due to its refractory nature, unlike Au and Ag, which would melt at lower temperatures.

Further information on the temperature-dependent optical behavior of TiN was addressed by *in situ* spectroscopic ellipsometry measurements during cyclic heating/cooling in high vacuum on epitaxial TiN films grown on MgO (001) [90]. The surface morphology before (figure 6(d)) and after repeated thermal cycling (figure 6(e)) exhibited a reconfiguration and an increase in roughness from ~ 4.93 to ~ 7.51 Å, while the columnar epitaxy of TiN on MgO was retained with only a slight decrease of the lattice constant along the (100) direction. The real and imaginary parts of the permittivity increased with temperature, similar to the results of [92] (figures 6(f) and (g)). In particular, less negative values of ε_1 indicated a less metallic response, while higher values of ε_2 a more absorptive behavior. Nevertheless, both quantities recovered their original room-temperature values upon cooling. The temperature-dependent permittivity data were employed to compute several relevant figures of merit (FOMs) for plasmonic applications. For example, the SPP propagation length at an air-TiN interface (equation (26)) decreased with temperature (in agreement with [92], figure 6(b)). An analogous effect with temperature was observed in two figures of merit for spherical TiN nanoparticles, i.e. the electric field intensity enhancement FOM and the heat generation FOM (figures 6(h) and (i)). Notably, the former showed a peak at ~ 570 nm at room temperature, which red-shifted to ~ 640 nm at ~ 1250 °C, while the latter exhibited a peak at ~ 515 nm irrespectively of the temperature. Despite both the FOMs decreased with temperature, the performance in terms of both field enhancement and heat generation was still adequate for high-temperature applications.

On the other hand, the stability of TiN upon thermal treatments was investigated in [87], where epitaxial 80 nm thick TiN films grown on Al_2O_3 (0001) single crystal substrates (figure 6(j)) were tested in medium (3×10^{-3} mbar) and high vacuum (2×10^{-6} mbar) conditions up to 1000 °C and 1400 °C, respectively. A prolonged (8 h) high-vacuum annealing, in particular, induced a morphological change in the TiN film structure due to the formation of low-index interfaces throughout the film and grain size increase (from ~ 76 to ~ 110 nm) at the expense of high-angle grain boundaries. This produced an elongation of grains along the [111] direction and spherodization of the columnar structure, thus increasing the surface roughness (figure 6(k)). However, neither oxidation in TiN nor inter-diffusion of the elements between the TiN film and the Al_2O_3 substrate occurred, as evidenced by electron energy dispersive mapping (figure 6(k)). Additionally, the film treated for 2 h in high vacuum did not exhibit any significant change in reflectivity

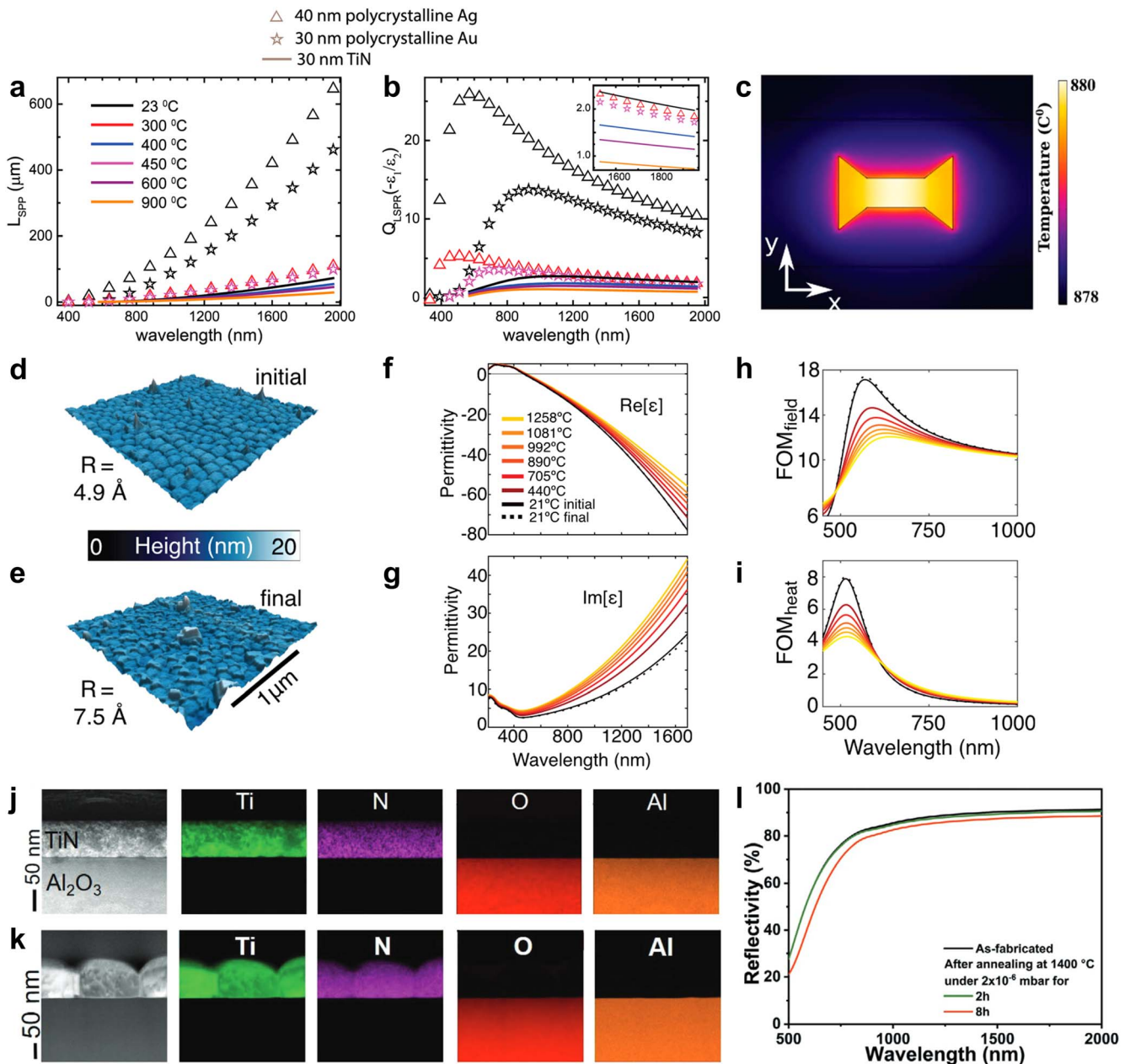


Figure 6. High-temperature optical properties of epitaxial TiN films. (a) SPP propagation length and (b) Q_{LSPR} of Ag, Au and TiN at different temperatures (23 °C–900 °C). (c) Thermal profile in a TiN diabolo antenna (maximum width = 235 nm and maximum height = 150 nm) under 61 mW irradiation power computed using temperature-dependent permittivity of TiN. Reproduced with permission from [92], Copyright 2017, American Chemical Society. (d) Surface morphology of TiN film grown on MgO(001) before and (e) after four heating/cooling cycles up to ~1200 °C. (f) Real part and (g) imaginary part of the relative permittivity of TiN on MgO(001) as a function of temperature and corresponding figures of merit for the electric field enhancement (h) and heat generation (i) for a spherical TiN nanoparticle in vacuum. Reproduced with permission from [90], Copyright 2017, American Institute of Physics. (j) Cross-sectional micrograph and corresponding elemental maps for pristine TiN thin film grown on Al_2O_3 (0001) and (k) the same after annealing at 1400 °C under high vacuum (2×10^{-6} mbar) for 8 h. (l) Specular reflectivity of pristine and thermally-treated TiN films on Al_2O_3 (0001). Reproduced with permission from [87]. Copyright 2021, Wiley-VCH.

compared to the as-deposited one, while a slight decrease was found for the film treated for 8 h (figure 6(l)), which corresponded to an increase in ϵ_2 . Since no oxidation effect was found, such minor changes in the optical quality of TiN were attributed to the surface roughness increase. As a result, this work showed the excellent thermal stability of TiN epitaxial films in vacuum, which is of great interest in applications such as thermophotovoltaics.

4.4. Ultrathin TiN films

The fabrication of epitaxial TiN films by DCMS has been recently pushed down to the limit of only a few nm, thus realizing ultrathin films. This is motivated by the growing interest in the so-called transdimensional materials (TDMs) [93], i.e. materials characterized by a thickness of only a few atomic layers that exhibit intermediate properties between 3D

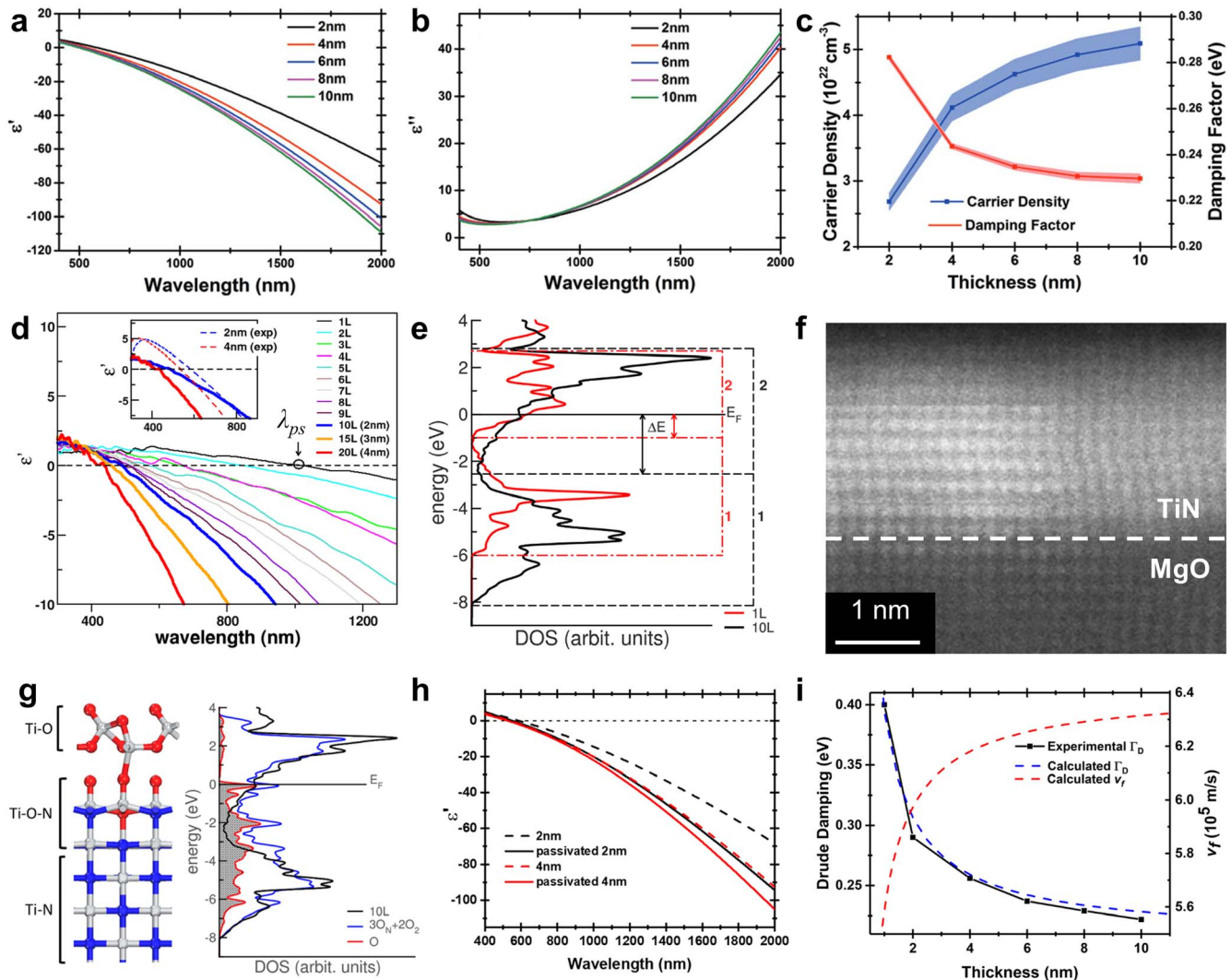


Figure 7. Optical properties of ultrathin TiN films epitaxially grown on MgO substrates. (a) Real and (b) imaginary parts of the dielectric function measured by spectroscopic ellipsometry. (c) Carrier density measured by Hall effect experiments and Drude damping factor retrieved by ellipsometry. (a)–(c) Reproduced with permission from [94]. Copyright 2017, Wiley-VCH. (d) Numerically simulated real part of the dielectric function as a function of the number of layers N_L and comparison with the experimental data for 2 nm and 4 nm thickness (inset). (e) Simulated density of states for 1-layer and 10-layer systems, where the dashed lines highlight the position with respect to E_F and the width of the two main group of energy bands (1, 2) responsible for the crossover wavelength in the visible range. (f) High-angle annular dark field scanning transmission electron microscopy image of a 2 nm TiN film on MgO substrate. (g) Geometry and density of states of the $3O_N + 2O_2$ configuration (total, blue line, and O-projected, shaded area) compared to the ideal unoxidized 10-layer case. (d)–(g) Reproduced with permission from [95]. Copyright 2018, American Chemical Society. (h) Comparison of the real part of the permittivity for unpassivated and 10 nm AlScN *in situ* passivated films. (i) Thickness-dependent Drude damping factor retrieved from ellipsometry measurements compared to the calculated one and Fermi velocity. (h)–(i) Reproduced with permission from [96]. Copyright 2022, American Chemical Society.

and 2D materials. In particular, plasmonic TDMs may offer unprecedented properties of dynamic tunability, energy transitions forbidden in their bulk counterparts, and enhanced nonlinearities [93]. To gain more insights into the field of TDMs, the group of Shalaev and Boltasseva has conducted a series exploratory studies on ultrathin TiN films epitaxially grown on MgO [94–96]. This was motivated by the possibility of fabricating continuous ultrathin TiN films down to 2 nm, while the same could not be achieved with traditional noble metals (i.e. Au and Ag) due to island formation at the first stages of growth.

In a first study, the authors investigated the permittivity of ultrathin TiN films with 2–10 nm thickness grown at 800 °C on MgO by reactive DCMS [94]. Such deposition conditions and the lattice matching between TiN and the substrate ensured the growth of highly metallic films (see also section 4.3). However, by decreasing the film thickness, the degree of metallicity decreased, as demonstrated by the increase of both the real and the imaginary part of the complex permittivity (figures 7(a) and (b), respectively). Hall measurements further revealed that the free electron concentration decreased with the film thickness (figure 7(c)), which was ascribed to the effect of the intrinsic surface

oxidation layer (i.e. 2 nm thick TiO_xN_y). Nevertheless, even the 2 nm thin films were characterized by a carrier density of $\sim 10^{22} \text{ cm}^{-3}$ and, therefore, by a good metallic quality. On the other hand, the Drude damping factor retrieved by ellipsometry (Γ_D) increased by decreasing the film thickness (figure 7(c)). This was ascribed to the presence of defects and surface scattering phenomena arising from a lower film thickness than the electron mean free path (~ 45 nm in bulk TiN) [97]. For the same reason, films thinner than 4 nm also exhibited a reduction of the plasma frequency.

In a follow-up study, the authors investigated more in detail the underlying effects occurring ultrathin TiN films by DFT simulations. In particular, systems from one to 20 monolayers (0–4 nm) of TiN(001) were simulated and compared to the experimental data (figure 7(d)). In agreement with previous results, a reduction in the metallic character of the films with the thickness was observed, which indicated a decrease of the electronic screening. This was further highlighted by the redshift of the crossover wavelength (λ_{ps} in figure 7(d)). To gain insights into that, the DOS of a one-layer (1 L) and 10-layer (10 L) systems were computed using an electromagnetic model taking into account quantum confinement effects (figure 7(e)). Both DOS plots featured bands mostly consisting of N(2p) orbitals below E_F (labelled with **1** in figure 7(e)) and bands mostly composed of Ti(t_{2g}) orbitals slightly hybridized with N(2p) crossing E_F and above (labelled with **2** in figure 7(e); see also figure 3(c)). By defining as ΔE the energy difference between the band **1** and E_F , which is associated with the screened plasma energy (E_{ps}), the 1 L system exhibited a decrease in ΔE compared to the 10 L one because of under-coordinated surface atoms, thus reducing the free electron charges. However, a systematic blueshift of theoretical λ_{ps} values compared to the experimental ones was found (see inset of figure 7(d)). Interface strain between the TiN ultrathin films and the MgO substrate was ruled out because of a very small lattice mismatch between the two materials ($\sim 0.7\%$), as evidenced by the lattice relaxation at the TiN/MgO interface (figure 7(f)). Therefore, by considering experimental evidence of surface oxidation by XPS results, the effect of O atoms in different configurations was evaluated. As a result, a new DOS plot was computed by considering the presence of both Ti–O bonds (labelled with O_2), forming a surface layer of TiO_2 , and O atoms in the N lattice (labelled with O_N), forming an intermediate TiO_xN_y layer between TiO_2 and TiN (figure 7(g)). The so-obtained DOS maintained a metallic character, but the additional oxygen orbitals produced localized states across E_F contributing to interband transitions, thus redshifting λ_{ps} . Therefore, the effect of surface oxidation considerably reduced the effective thickness of TiN and allowed reaching a quantitative agreement between experimental and simulated data of permittivity.

A further study by the same group shed more light on the matter of ultrathin TiN films by disentangling the contribution of surface oxidation and quantum confinement effects [96]. This was achieved by passivating the TiN surface with an epitaxial layer of AlScN grown *in situ* with the same reactive DCMS apparatus. Subsequent ellipsometric experiments

revealed that the passivated ultrathin (1–10 nm) TiN films were more metallic than the unpassivated counterparts and exhibited a negative increase of the real part of the permittivity (figure 7(h)). The thickness dependence of the plasma frequency of the passivated films was therefore investigated by a theoretical model developed for plasmonic TDMs that explicitly considers a vertical confinement layer thickness d [98, 99]. As a result, a modified expression of the 3D Drude plasma frequency (with a \sqrt{d} dependence) allowed a quantitative description of the experimental data. Furthermore, a modified expression for the Drude damping taking into account the films thickness was also found. The latter increased by decreasing the film thickness (while the computed Fermi velocity decreased) because of surface scattering and it quantitatively followed the experimental data (figure 7(i)).

The aforementioned results on ultrathin TiN films may therefore pave the way toward the exploitation of new optical phenomena arising from enhanced light–matter interactions. Follow-up studies devoted to ultrathin plasmonic meta-surfaces exploiting quantum confinement effects could be thus expected [100].

5. TiN by PLD

5.1. Fundamentals of PLD

Pulsed Laser Deposition (PLD) is a PVD technique where the material to be deposited is brought to the vapor state by means of a physical process, which is known as laser ablation [101–103]. A variety of materials and compounds can be deposited, both inorganic (metals, metal oxides, semiconductors, ceramics) and organic (polymers, biomolecules) [101, 104–109]. A high-energy pulsed laser beam hits a solid target material, which is immediately vaporized at the surface. Part of the energy absorbed by the vaporized species is converted into kinetic energy, so that they are spontaneously ejected towards the substrate placed at a proper distance (typically a few centimeters), where the growth takes place after particles condensation [110]. To activate this process and pursue film growth with reasonable deposition rates ($>1 \text{ \AA/pulse}$), a threshold value for the laser energy density (i.e. laser fluence in J cm^{-2}) must be reached [102]. This ablation threshold is a function of the properties of the material considered (i.e. cohesive energy, thermal conductivity) and varies with the deposition parameters, namely laser wavelength or laser spot size. The ablated flux (including atoms, ions, molecules, electrons, and small aggregates) expands in a supersonic plasma with a characteristic plume, whose shape and length of extension depend on the peculiar laser-target and laser-plasma interaction. Laser ablation can be performed either in vacuum or in the presence of a background gas, which can be inert or reactive according to the properties desired in the growing film, the latter case known as reactive PLD [111]. A complete treatment of the deposition and plume dynamics is rather complex, as generation, expansion and condensation of the plasma are nonlinear processes and occur in an out-of-equilibrium condition. The

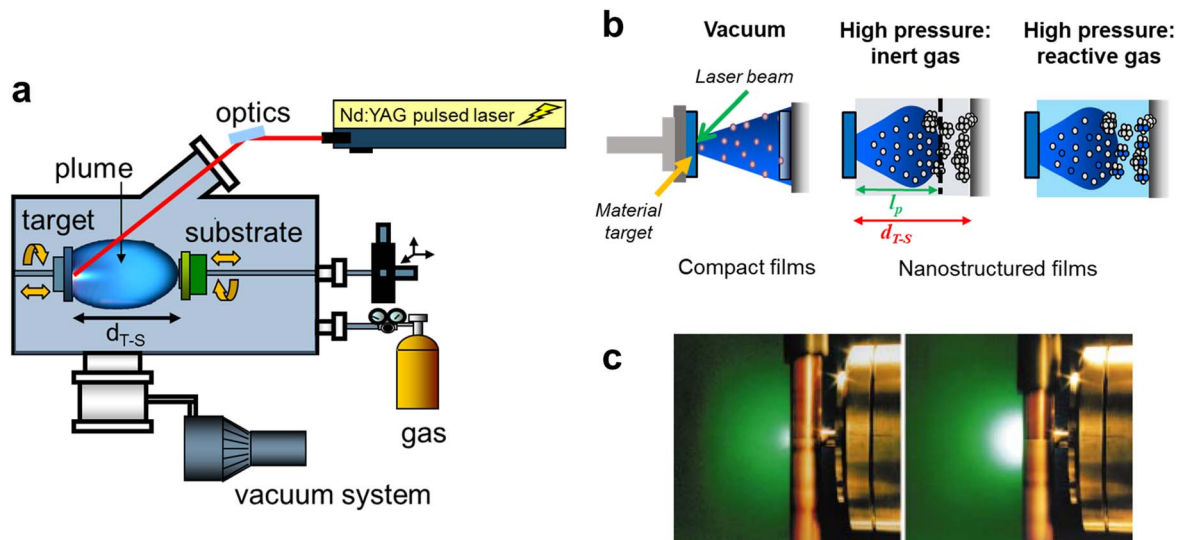


Figure 8. Typical PLD set-up and deposition mechanisms. (a) Scheme of a PLD apparatus: vacuum chamber equipped with target and substrates roto-translation motors, pumping systems, gas inlet and flow controllers. The high-intensity laser source, i.e. Nd:YAG pulsed laser emitting at fundamental wavelength or higher harmonics, is typically placed close to the chamber and is focused to the target with a series of optical elements. (b) Scheme of the deposition process performed in vacuum and at high pressure (with inert or reactive gases) with a consequent modification of the film properties (i.e. morphology) with indication of the plume length (l_p) and the target-to-substrate distance (d_{T-S}). (c) Change in the visual appearance of a Cu ablation plume propagating into vacuum (left image) and crossed with an N_2O gas pulse (right image). Reproduced with permission from [115]. Copyright 2000, The American Physical Society.

possible physical mechanisms involved at each step are manifold (single or multi-photon absorption, desorption or collisional, thermal, electronic and mechanical phenomena) [102], and their detailed discussion is beyond the scope of this work. Moreover, the scale of pulse duration, ranging from nanoseconds (ns-PLD, most employed) to femtoseconds, determines the deposition regimes, which consequently affect the mechanism of ablation [112–114]. The interested reader can refer to [101, 102, 115] for a more complete description.

Figure 8(a) reports a simplified scheme of a typical PLD apparatus. Laser pulses are focused through an optical system onto the target surface, hosted with the substrate inside a vacuum chamber. The latter is equipped with a pumping system to reach the high vacuum condition required ($\sim 10^{-2}$ Pa). Consequently, a background gas (Ar, O_2 , N_2) can be introduced through a gas inlet, at controlled pressure and flow, to perform depositions in inert or reactive atmospheres. The target and substrate are subjected to roto-translation by means of remote-controlled motors, to ensure uniform target ablation and to grow homogeneous deposits over few centimeters of area. The most critical parameters that affect not only the plume expansion dynamics, but also the growth mechanisms, are the distance between target and substrate (d_{T-S}), the laser fluence and the background atmosphere (type and pressure). Optionally, a substrate heater can be implemented to help atomic re-arrangement and organization during film growth.

The laser fluence is actually the ratio of the laser beam energy over the spot size on the target and plays the major role in determining the ablation dynamics. It can be adjusted by operating on the laser beam optics or directly on the beam energy. For a ns-PLD, the instant power varies between 10–100 MW, with spot area of few mm, resulting in several J

cm^{-2} . Once the fluence is fixed, the background gas and its pressure value define the plume shape and the degree of ionization, which eventually determine the deposition regime of the growing films (figure 8(b)). A non-dimensional parameter, called L , can be defined as:

$$L = \frac{d_{T-S}}{l_p} \quad (27)$$

where l_p is the visible plume length at each laser pulse [110]. This parameter allows to discriminate among different growth modes. The low-pressure or vacuum-like regime is characterized by $L < 1$ (figure 8(b), left). In this case, the substrate is placed within the plume length, which is confined at the shock front. Ablated species from the target reach the substrate almost unperturbed (no collisions) and gain high kinetic energy (10–50 of eV/atom) [116]. The film is deposited atom-by-atom, resulting compact, bulk-like and usually preserving stoichiometry as the composition of the target. On the other hand, the high-pressure regime is characterized by $L > 1$ (figure 8(b), center). In this case, particles ejected from the target transfer mechanical momentum to the background inert gas due to the increased probability of collisions thus leading to spatial confinement of the plasma plume, well defined by a plume edge, with a clearly visible expansion front. Aggregates and clusters can form directly during flight in the gas phase prior to the substrate deposition. Consequently, kinetic energies decrease (fractions of eV/atom) and cluster-assembled nanostructures can be obtained [110, 117]. The intermediate situation ($L \sim 1$), where the substrate is at the plume front, favors the growth of hierarchical morphologies [110]. Moreover, if the background gas can chemically interact with the ablated species (figure 8(b), right; reactive PLD), e.g. oxygen-rich or nitrogen-rich atmospheres with

oxides/nitrides, the films would result with a different final stoichiometry. Figure 8(c) shows the typical appearance of the plasma plume in vacuum or in high background gas.

Among the main drawbacks of the technique, there is the impossibility to deposit over large area in lab-scale apparatus, with a consequent loss in thickness uniformity. In addition, molten particles directly detaching from the target surface are present in the deposited film as protrusions from hundreds of nanometers to micrometers dimension, increasing the roughness and, in most of the cases, negatively affecting structural and optoelectronic properties of thin-film material. Crystallographic defects or residual stresses in the deposited film are possible unwanted outcomes, resulting from the high kinetic energies of the ablated particles impinging at the substrate.

A fundamental advantage of PLD with respect to sputtering is the stoichiometric transfer of material from target to substrate with non-thermal kinetic energies (up to ~ 100 eV/atom), thus with the possibility to deposit at room temperature on a variety of substrates (from common soda lime glass to low-melting polymers) [116]. If the background pressure is kept sufficiently low (< 1 Pa), the ejected flux is composed primarily by atoms, ions and molecules to grow layer-by-layer, a feature shared by much more complex techniques, such as MBE. Another key aspect is the unique capability of PLD, absent in sputtering, to widely control the morphology during the synthesis stage, i.e. from compact to nanoporous architectures.

5.2. Highly metallic TiN films by PLD

PLD allows to deposit highly energetic species in vacuum or low-pressure gas, enabling the formation of high-quality surfaces and less-defective films while keeping low temperature at the substrate. Eventually, this leads to reduced residual thermal strains incurring after post-deposition cooling due to lattice mismatch between the film and the substrate. Hence, PLD is promising for obtaining TiN with high metallicity and good material quality, as recently demonstrated by Sugavaneshwar *et al* [9]. In their pioneer work, excellent metal-like and plasmonic behaviour, competing to gold, was reached in TiN films grown at room temperature (25°C) on inexpensive substrates (SiO_2/Si and flexible polymers) by ablating a TiN target in vacuum ($6 \cdot 10^{-4}$ Pa) at fluence of 6 J cm^{-2} . Optical properties (ϵ_1 and ϵ_2) of TiN films are shown in figures 9(a), (b). Metallicity in TiN increased at higher deposition rates (from 0.03 to 0.1 \AA s^{-1}), although exhibiting lower plasmonic performances compared to gold in terms of the plasmonic quality factor for LSPR (figure 9(c) and equation (19)). A significant advancement has been made for the integration in real devices by depositing TiN of 150 nm on poly-methyl methacrylate (PMMA) with optimal metal-like properties (figures 9(d), (e)). TiN films on PMMA exhibited lower ϵ_1 than the corresponding films deposited on Si/SiO_2 , indicating a loss in metallicity. This was ascribed to a degraded structural quality when growing on the rough surface of PMMA. However, ϵ_2 was lower than that of TiN on Si/SiO_2 (figure 9(e)). The good metallic quality of the

films was also confirmed by the visual gold-like appearance of the films in all the investigated conditions (inset in figure 9(d)). The authors further showed the feasibility of TiN growth by PLD on organic flexible free-standing poly-ethylene terephthalate (PET) substrates (figure 9(f)), therefore significantly widening the potential applicability of this material.

Notably, the growth with highly energetic species enabled by PLD has been also exploited in [118] to produce epitaxial TiN thin films (75 nm) on $c\text{-Al}_2\text{O}_3$ (0001) at 450°C (medium temperature, MT), 650°C (high temperature, HT) and at room temperature (RT). The latter is remarkable since epitaxy usually requires high thermal energies to favor atom diffusion and rearrangement in ordered structures (section 4.3) [11, 57, 119–123]. Despite higher residual strains and defectivity due to the insufficient thermal energy at the unheated substrate, RT epitaxial growth has been fulfilled (figure 9(g)) under the epitaxial relationship $(111)\text{TiN}/(0001)\text{Al}_2\text{O}_3$ and $(\bar{1}\bar{1}0)\text{TiN}/(10\bar{1}0)\text{Al}_2\text{O}_3$. Zone axes at film/substrate evidenced a 4° tilt due to partial grain misalignment, while HT deposition produced an almost perfect alignment and excellent material quality. Nevertheless, the latter was also associated with the formation of unwanted titanium oxynitride (TiO_xN_y) phases at the boundary with the substrate that acted as ‘weak point’ for the residual strain propagation in the film. Such interlayer was formed as a result of a thermally-driven reaction of the Al_2O_3 surface with the incoming species, leading to intermixing with O and N and thus to a three monolayer-thick pseudomorphic TiO_xN_y layer (figure 9(h)). To determine the defect density in TiN lattices, Raman spectroscopy is a valuable tool as Raman signals in TiN are activated by defects (nitrogen or titanium vacancies), allowing to estimate the stoichiometry by investigating bands associated to acoustic and optical modes (more detailed discussion is available elsewhere [124–126]). Raman analysis on all the investigated films revealed an increase of N and Ti vacancies by decreasing the growth temperature, as shown by the drop in intensity of transverse optical (TO) and longitudinal acoustic (LA) vibrations (figure 9(i)). Both Ti and N vacancies produce additional scattering for free carriers and, consequently, degrade the optoelectronic performance of metallic TiN. Therefore, the overall increase in relative intensities in RT-grown films was ascribed to substoichiometry. However, the latter exhibited comparable electrical resistivity to that of films deposited at high temperature (i.e. $\sim 55 \mu\Omega \text{ cm}$ versus $\sim 22 \mu\Omega \text{ cm}$, respectively), therefore highlighting the possibility of achieving satisfactory conductivity in TiN despite the absence of substrate heating.

5.3. Optically-absorbing titanium oxynitride or nanoporous films

TiN usually presents a relatively broad absorption peak that extends from the visible toward the near-infrared (NIR) range of the electromagnetic spectrum (figure 3(d)). Such optical absorption can be further engineered to realize broadband solar absorbers by introducing oxygen in a controlled form, thus realizing titanium oxynitrides (TiO_xN_y) featuring additional interband transitions associated to O 2p orbitals (figure 7(g)).

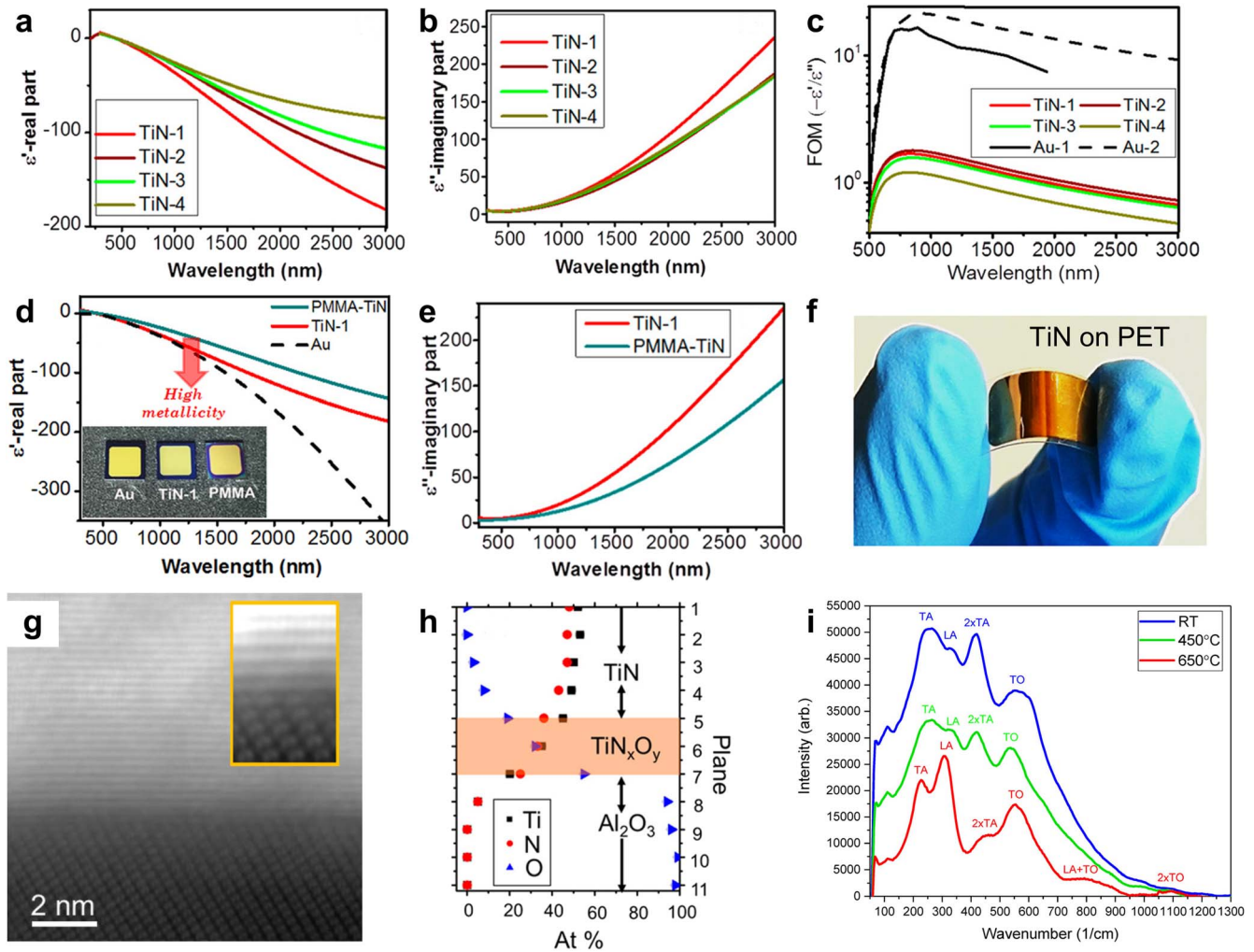


Figure 9. TiN films prepared by PLD with highly metallic properties. Comparison of the real (a) and imaginary (b) permittivity of TiN films deposited by PLD with decreasing deposition rate (0.1, 0.07, 0.05, and 0.03 Å s⁻¹ for TiN-1, TiN-2, TiN-3, and TiN-4, respectively). (c) Figure of merit (FOM) $-\epsilon'/\epsilon''$ of different TiN films compared with Au data extracted from literature. Real (d) and imaginary (e) permittivities of TiN films deposited on SiO₂/Si (TiN-1) and PMMA (PMMA-TiN) substrates. (f) PLD-TiN film on a PET substrate. (a)–(f) Reproduced with permission from [9]. Copyright 2017, The American Chemical Society. (g) HAADF image of room-temperature epitaxial TiN on c-Al₂O₃ with zone-axis aligned with substrate. (h) Elemental distribution (% at) of Ti, N, and O along the marked planes (1 $\bar{1}$ 1) showing the formation of three monolayer thick TiN_xO_y at the interface. (i) Raman spectra of epitaxial TiN samples grown at different temperatures (RT versus HT). The lower intensities for higher quality film are expected as vibrational scattering modes are enhanced with higher vacancy concentrations. (g)–(i) Reproduced from [118]. Copyright 2017, The American Chemical Society.

Yamaguchi *et al* in [10] addressed the deposition of TiO_xN_y from a TiO₂ target *via* PLD by controlling Ti/O/N ratios at fluence of 3.5 J cm⁻² with the assistance of a nitrogen plasma, whose reactivity at non-equilibrium situation can provide N incorporation. The aim was to efficiently regulate the introduction of N in TiO₂, rather than O in TiN, which is more complex to manage as TiN oxidation into TiO₂ is energetically favored. The quantity of N and O within the films could be finely adjusted with deposition parameters, *i.e.* emission current of the nitrogen plasma (figure 10(a)), allowing to reach noticeable absorption coefficients at visible wavelengths (up to 40 μm⁻¹ in 400–700 nm) required for the target application in flat-panel displays (figure 10(b)). The absorption coefficient could be further improved by varying the plasma voltage (figure 10(c)). The mechanism underlying

such an effect was a contamination from W filaments of the set-up occurring at higher discharge voltages, thus leading to W doping. The so-obtained W-doped TiO_xN_y, compared to other widespread black absorbers (*i.e.* graphite), represented a balanced compromise between intensified absorption and good film uniformity (reduced surface roughness, maintained at 0.67 nm). A high film uniformity was indeed critical to prevent unwanted light scattering and reflections, thus lowering absorption capability (figure 10(d)). The calculated electronic band structure of TiO_xN_y and W-doped TiO_xN_y is schematized in figure 10(e). The superior optical absorption described so far was the result of a combination of intraband and interband transitions involving O/N 2p and Ti 3d. W doping produced additional intraband excitation pathways from W 5d states to the Ti/W d states, increasing the

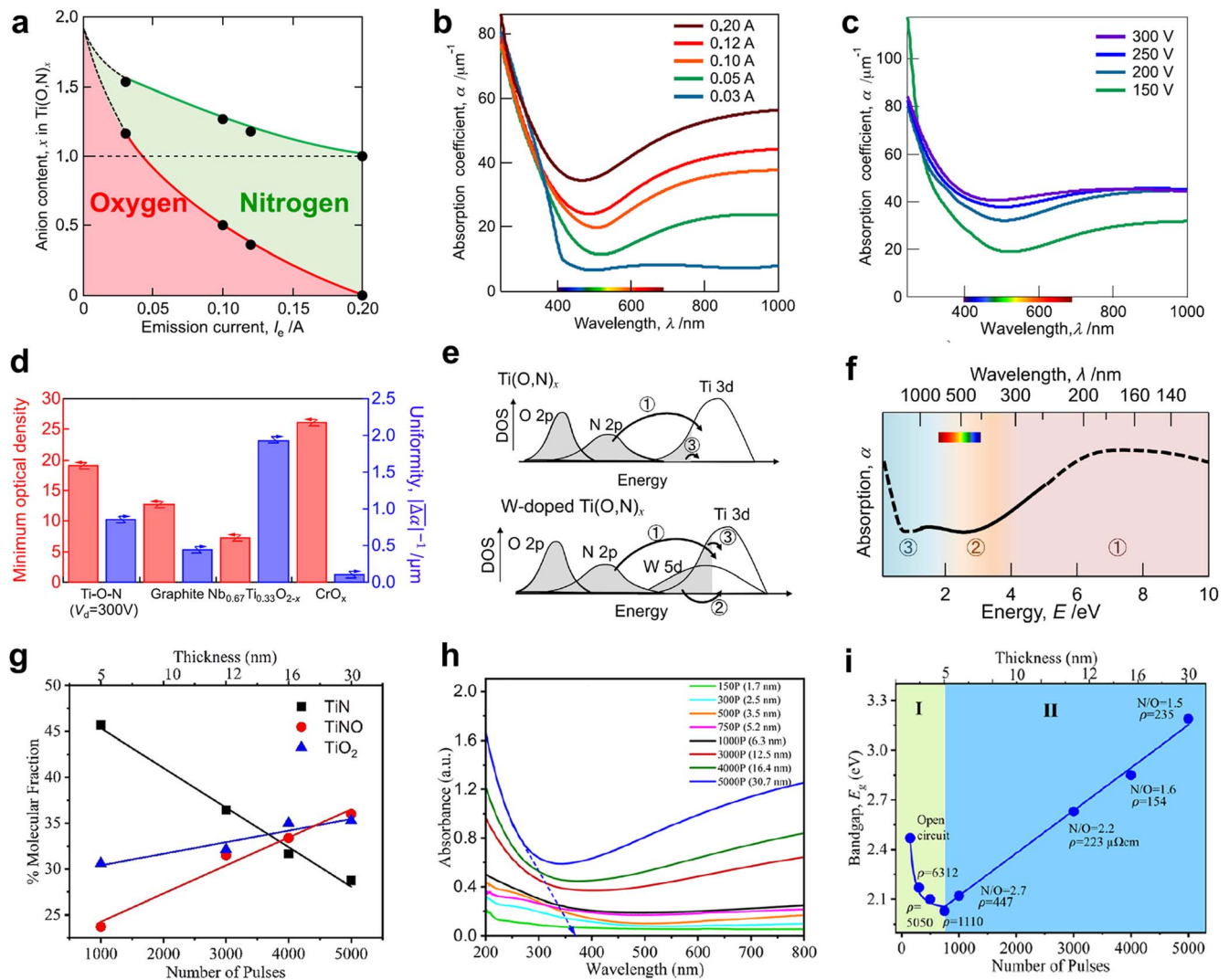


Figure 10. Titanium oxynitrides films prepared by PLD. Anion content (a) and absorption coefficient (α) of the TiO_xN_y thin films deposited by varying the extraction current $I_e = 0.03$ – 0.20 A at constant discharge voltage $V_d = 150$ V (b) and by varying the discharge voltage $V_d = 150$ – 300 V at fixed extraction current $I_e = 0.10$ A (c). (d) Comparison of the absorption in the visible range (400–650 nm) of TiO_xN_y thin film prepared at $V_d = 300$ V compared to other reference absorber materials. (e) DOS sketches of (W-doped) TiO_xN_y: ① interband transition from O/N 2p states to Ti 3d (and W 5d when doped) states, ② intraband transition from W 5d states to the Ti/W d states, and ③ intraband transition in the Ti/W d states. (f) Calculated wide-range absorption spectrum of W-doped TiO_xN_y. (a)–(f) Reproduced with permission from [10]. Copyright 2020, Elsevier B.V. (g) Molecular fractions of TiN, TiON (referred in the graph as TiNO), and TiO₂ in the thin films as a function of the number of pulses. TiN content reduces with larger extent (35%) with respect to the increase in TiON and TiO₂ phases (50% and 15% respectively). (h) Absorbance as a function of wavelength for the TiON films made using 150 to 5000 laser pulses. (i) Bandgap of TiN/TiON films as a function of the number of pulses, with indication of resistivity ρ and N/O ratio. (g)–(i) Reproduced with permission from [127]. Copyright 2023, American Chemical Society.

absorption at middle energies, i.e. between 2 and 4 eV (figure 10(f)).

Titanium oxynitrides prepared by PLD have been recently studied for photocatalytic applications [127, 128]. For example, in the work of Roy *et al* [127], surface oxidation from TiN to TiO_xN_y could be regulated by tuning the number of laser pulses (150–5000 shots, i.e. ultra-short depositions) during ablation of TiN targets in vacuum to achieve ultrathin thickness (5–30 nm). Oxidation in the films increased by increasing the deposition time (figure 10(g)). This effect was ascribed to the time-dependent diffusion of residual O₂ species in the chamber, producing O incorporation in the anion sites of the cubic TiN structure, therefore leading to TiO_xN_y.

Therefore, surface oxidation could be mitigated by lowering the deposition time. For the same reason, the so-obtained TiO_xN_y films exhibited a thickness-dependent optical absorption with a semiconducting behavior, i.e. the presence of a bandgap (E_g), unlike metallic TiN (figure 10(h)). Moreover, the bandgap value (E_g) exhibited a V-shaped trend with respect to the number of pulses (figure 10(i)). This was explained by means of two distinct growth regimes depending on the film thickness. In the first region (i.e. low thickness), a bandgap decrease from 2.47 to 2.03 eV was associated to an island-like regime (with average dimension D , therefore with incomplete substrate coverage) to continuous films according to the empirical trend $E_g \sim 1/D^3$. In the second region, a

linear increase of the bandgap (from 2.03 to 3.21 eV) was associated to progressive oxidation of the films, which first occurred by a controlled O incorporation in the cubic structure of TiO_xN_y and, subsequently, by formation of dispersed TiO_2 domains. These results, however, differ from those found in investigations of the epitaxial growth of ultrathin films by magnetron sputtering (section 4.4), which instead demonstrated the formation of continuous films even for few-layer thickness. Nevertheless, the bandgap engineering presented by Roy *et al* [127] may open new paradigms in the exploration of TiO_xN_y for photocatalysis.

The great tunability of film morphology directly during the growth by changing the PLD parameters has been exploited to synthesize nanoporous TiN or TiO_xN_y films. In particular, the film morphology evolved from compact-like to nanoporous tree-like by increasing the background gas (N_2/H_2 mixture) pressure ablating a TiN target [129, 130]. This strategy was first used to prepare hierarchical TiN nanostructures combined with Pt nanoparticles as electrodes for fuel cells, which offered a high surface area and high stability under repeated electrochemical cycling [130]. More recently, the same approach was investigated to realize broadband solar absorber films [129]. In particular, the film deposited in vacuum was characterized by a compact and columnar structure (figure 11(a)), which evolved toward a nanoparticle-assembled nanoporous structure by introducing a background N_2/H_2 gas at increasing pressure up to 100 Pa (figures 11(a) and (b)). The use of a N_2/H_2 gas aimed at favoring the Ti–N bond formation during the growth leading to TiN cubic crystal structure, as confirmed by XRD analysis. Nevertheless, EDX analysis revealed a significant presence of O in the films, i.e. $\sim 30\%$ for the compact films and $\sim 50\%$ for the nanoporous ones (as shown for the 100 Pa deposition in figures 11(d)–(e)). This effect was ascribed to the low density and porosity of the films that both favor the saturation of N vacancies by exposure to oxygen. The so-obtained films were further characterized by UV–visible–NIR spectroscopy (250–2000 nm wavelength range) and Fourier-transform infrared (FTIR) spectroscopy (1330–25000 nm range). The optical spectra of the film deposited in vacuum (figure 11(f)) revealed the typical features of bulk TiN, i.e. high reflectance for $\lambda > 600$ nm (see also figure 3(c)). On the contrary, the absorbance monotonically increased with the background gas pressure (figure 11(f)). The nanoporous films exhibited a broadband absorbance in the full investigated range, with maxima at ~ 500 nm, ~ 1000 nm and $\sim 13\,000$ nm, which was ascribed to the nanoporous morphology, leading to light trapping by scattering effects and hybridization of plasmon resonances, and to the oxynitride chemical composition. The potential performance of the films as broadband solar absorbers in solar-thermal applications was assessed by temperature measurements under moderately-concentrated solar-simulated light (1.3–17 Suns) using an IR thermal camera (figure 11(g)). All the investigated films exhibited higher steady-state temperatures compared to a reference Ti plate substrate. Moreover, the generated temperatures increased with the deposition pressure and the maximum value of ~ 475 °C was found for the film deposited at 100 Pa under 17

Suns. No significant degradation nor oxidation was found upon thermal cycling, which were performed in inert Ar atmosphere. By computing the spectrally-averaged absorbance and emittance [131, 132], the thermal transfer efficiency of the films was evaluated, finding the maximum value of $\sim 79\%$ for the film deposited at 100 Pa under 1.3 Suns. The thermal transfer efficiency decreased with the irradiation intensity likely due to radiative losses, which in turn are related to a high emissivity in the medium-IR range. Therefore, future works in this regard may address the optimization of the optical properties of nanoporous TiO_xN_y films to realize spectrally-selective absorbers, such as by realizing compact/porous multi-layers in the same PLD process [133].

6. Conclusions and perspectives

TiN has emerged as a promising replacement for Au as a plasmonic material by virtue of its tunable optical response, diverse nanofabrication routes, and refractory nature. This review focused on the use of magnetron sputtering and PLD as PVD techniques because of valuable advantages in light of large-scale development of plasmonic TiN-based devices. On the one hand, magnetron sputtering is a widely-available technique compatible with industrial processes and can lead to highly metallic TiN thin films. Moreover, this method has recently been employed to realize unprecedented ultrathin (< 10 nm thickness) films with good metallic quality, which is not feasible with traditional plasmonic metals. On the other hand, PLD allows tuning the material morphology, composition and structure to produce nanoporous or partially-oxidized TiN materials with uncommon optical features, such as broadband absorption in the whole solar spectrum. In this regard, a thorough knowledge of the basic principles of magnetron sputtering and PLD is mandatory to design TiN-based nanomaterials with engineered optical properties. Furthermore, spectroscopic ellipsometry is a prominent optical technique to retrieve the complex permittivity of the so-realized materials and to predict the material resistivity and the plasmonic performance by Drude–Lorentz modelling, although less suitable for highly porous and light-absorbing films.

The rising interest in TiN and the consequent results achieved in the last decade are encouraging in the view of upscaling plasmonic applications based on this material. Further research in this regard is therefore expected according to different directions. For example, ternary TMNs such as $\text{Ti}_x\text{Ta}_{1-x}\text{N}$ and $\text{Ti}_x\text{Sc}_{1-x}\text{N}$ have already revealed a great tunability of plasmonic resonances in a wide range of wavelengths, i.e. 150–1500 nm [134, 135]. In particular, the possibility of integrating simple metals, such as Mg or Ca [136], in TMNs is highly attractive in terms of realizing realistic plasmonic devices with limited amounts of critical raw materials [137]. On the other hand, the controlled alteration of TiN stoichiometry with a controlled O content, realizing oxynitrides with variable composition (TiO_xN_y), is increasingly being investigated due to the possibility of achieving the so-called double epsilon-near-zero (2ENZ)

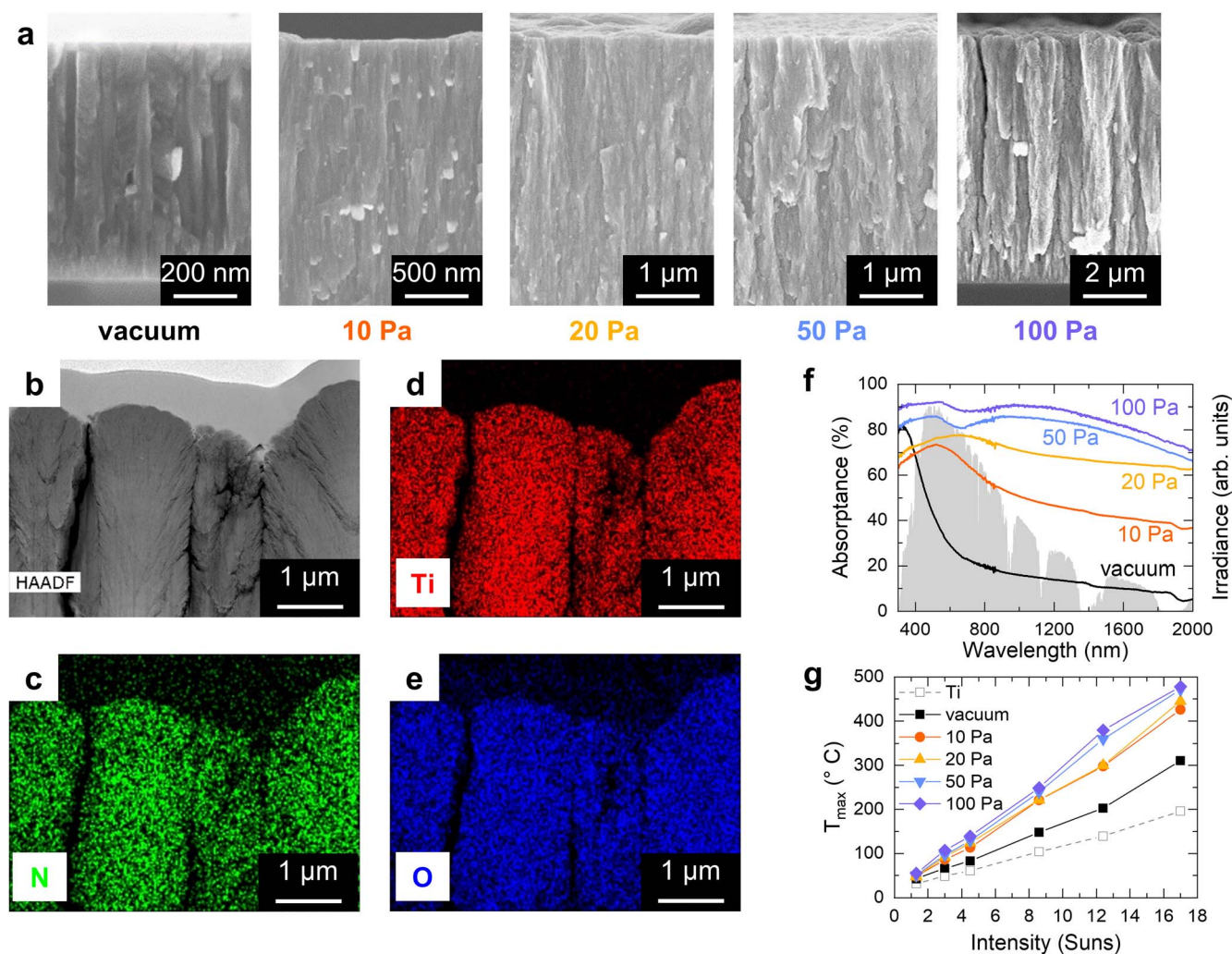


Figure 11. Nanoporous TiO_xN_y films broadband solar absorbers. (a) Morphological evolution (cross-sectional SEM images) of the films by increasing the background gas (N₂/H₂) pressure from vacuum to 100 Pa. (b) High-angle annular dark-field STEM (HAADF-STEM) image and corresponding EDX mapping of N (c), Ti (d), and O (e) for a film deposited at 100 Pa. (f) Optical absorbance of the TiO_xN_y films compared to the standard AM 1.5 G solar irradiance. (g) Steady-state temperatures of the films under solar-simulated light (1.3–17 Suns) measured by an IR thermal camera. Reproduced from [129]. CC BY 4.0.

behaviour. This can potentially lead to broadband optical absorption and multiple plasmonic resonances with a wide range of applications [138].

From the standpoint of nanoengineered surfaces, compact thin films have mostly been addressed to tune the permittivity of TiN and they can be easily investigated by spectroscopic ellipsometry. Recent results, however, have shown the possibility in realizing ultrathin film based on TiN [96], also known as transdimensional materials [93, 100]. Further investigations on this subject are likely expected, for example assessing the potentialities of other TMNs, such as ZrN [139], which exhibits lower optical losses compared to TiN, or the aforementioned ternary systems. Magnetron sputtering could still be conveniently employed as a fabrication technique, for example by simply choosing a suitable target material.

On the other hand, the information on the optical constants of TiN gained through the optical analysis of compact films can give valuable information to realize more complex

nanostructures, such as plasmonic metasurfaces [140, 141]. TiN represents a suitable material choice to design meta-atoms with desired morphology and to achieve broadband optical absorption even under severe irradiation conditions, while the counterparts made of Au would undergo melting [57]. In this regard, plasmonic metasurfaces based on TiN can lead to substantial heating effects, thus generating temperatures of ~500 °C under moderate light irradiation, which are critical in solar-energy conversion applications such as thermophotovoltaics [142] or gas-phase photothermal catalysis [143]. The latter is a particularly active field of research and could greatly benefit from the development of TiN-based nanostructures and metasurfaces to reach appreciable reaction rates in industrially- or environmentally-relevant chemical reactions [144, 145].

In light of these considerations, this review might be beneficial for other scientists interested not only in fundamental structure–property relationship in TiN nanomaterials, and in general in TMNs, but also in the realization of

plasmonic devices based on TiN nanostructures or meta-surfaces, which could bring significant progress in the whole field of plasmonics.

Acknowledgments


LM, MA, ŠK, and AN acknowledge the support from the Operational Programme Research, Development and Education—European Regional Development Fund, project no. CZ.02.1.01/0.0/0.0/15_003/0000416 of the Ministry of Education, Youth and Sports of the Czech Republic, and from the Czech Science Foundation (GACR) through the project 22-26416S. ŠK acknowledges the support of the Czech Science Foundation project GACR-EXPRO, 19-27454X. ALB acknowledges funding by the National Recovery and Resilience Plan (NRRP), Mission 4 Component 2 Investment 1.3—Call for tender No. 1561 of 11.10.2022 of Ministero dell'Università e della Ricerca (MUR), funded by the European Union—NextGenerationEU; and by project code PE0000021, Concession Decree No. 1561 of 11.10.2022 adopted by Ministero dell'Università e della Ricerca (MUR), CUP D43C22003090001, Project title 'Network 4 Energy Sustainable Transition—NEST'. A.N. acknowledges the support from the Project CH4.0 under the MIUR program "Dipartimenti di Eccellenza 2023-2027" (CUP: D13C2200352001).

Data availability statement

No new data were created or analysed in this study.

ORCID iDs

Luca Mascaretti  <https://orcid.org/0000-0001-8997-7018>

Cristina Mancarella  <https://orcid.org/0000-0003-3864-5819>

Andrea Li Bassi  <https://orcid.org/0000-0002-1265-4971>

References

- [1] Patsalas P, Kalfagiannis N, Kassavetis S, Abadias G, Bellas D V, Lekka C and Lidorikis E 2018 Conductive nitrides: growth principles, optical and electronic properties, and their perspectives in photonics and plasmonics *Mater. Sci. Eng. R* **123** 1–55
- [2] Jamal T, Nimmagadda R and Bunshah R F 1980 Friction and adhesive wear of titanium carbide and titanium nitride overlay coatings *Thin Solid Films* **73** 245–54
- [3] Peng Z, Miao H, Qi L, Yang S and Liu C 2003 Hard and wear-resistant titanium nitride coatings for cemented carbide cutting tools by pulsed high energy density plasma *Acta Mater.* **51** 3085–94
- [4] Sero A P, Completo C, Colaço R, dos Santos F, da Silva C L, Cabral J M S, Araújo H, Pires E and Saramago B 2009 A comparative study of titanium nitrides, TiN, TiN_{0.8}N and TiCN, as coatings for biomedical applications *Surf. Coat. Technol.* **203** 3701–7
- [5] Nemati A, Saghafi M, Khamseh S, Alibakhshi E, Zarrintaj P and Saeb M R 2018 Magnetron-sputtered Ti_xNy thin films applied on titanium-based alloys for biomedical applications: composition-microstructure-property relationships *Surf. Coat. Technol.* **349** 251–9
- [6] Niyomsoan S, Grant W, Olson D L and Mishra B 2002 Variation of color in titanium and zirconium nitride decorative thin films *Thin Solid Films* **415** 187–94
- [7] Kafizas A, Carmalt C J and Parkin I P 2013 CVD and precursor chemistry of transition metal nitrides *Coord. Chem. Rev.* **257** 2073–119
- [8] Ghantasala S B and Sharma S 2023 Magnetron sputtered thin films based on transition metal nitride: structure and properties *Phys. Status Solidi A* **220** 2200229
- [9] Sugavaneshwar R P, Ishii S, Dao T D, Ohi A, Nabatame T and Nagao T 2018 Fabrication of highly metallic TiN films by pulsed laser deposition method for plasmonic applications *ACS Photon.* **5** 814–9
- [10] Yamaguchi M, Ishii A, Oikawa I and Takamura H 2020 Black titanium oxynitride thin films prepared by nitrogen plasma-assisted pulsed laser deposition for flat-panel displays *Appl. Surf. Sci.* **534** 147616
- [11] Maurya K C, Shalaev V M, Boltasseva A and Saha B 2020 Reduced optical losses in refractory plasmonic titanium nitride thin films deposited with molecular beam epitaxy *Opt. Mater. Express* **10** 2679–92
- [12] Langereis E, Heil S B S, van de Sanden M C M and Kessels W M M 2006 In situ spectroscopic ellipsometry study on the growth of ultrathin TiN films by plasma-assisted atomic layer deposition *J. Appl. Phys.* **100** 023534
- [13] Van Bui H, Kovalgin A Y and Wolters R A M 2013 On the difference between optically and electrically determined resistivity of ultra-thin titanium nitride films *Appl. Surf. Sci.* **269** 45–9
- [14] Naik G V, Shalaev V M and Boltasseva A 2013 Alternative plasmonic materials: beyond gold and silver *Adv. Mater.* **25** 3264–94
- [15] Patsalas P, Kalfagiannis N and Kassavetis S 2015 Optical properties and plasmonic performance of titanium nitride *Materials* **8** 3128–54
- [16] Guler U, Shalaev V M and Boltasseva A 2015 Nanoparticle plasmonics: going practical with transition metal nitrides *Mater. Today* **18** 227–37
- [17] Brongersma M L, Halas N J and Nordlander P 2015 Plasmon-induced hot carrier science and technology *Nat. Nano* **10** 25–34
- [18] Besteiro L V, Yu P, Wang Z, Holleitner A W, Hartland G V, Wiederrecht G P and Govorov A O 2019 The fast and the furious: ultrafast hot electrons in plasmonic metastructures. size and structure matter *Nano Today* **27** 120–45
- [19] Khurgin J B 2020 Fundamental limits of hot carrier injection from metal in nanoplasmonics *Nanophotonics* **9** 453–71
- [20] Gui L, Bagheri S, Strohhfeldt N, Hentschel M, Zgrabik C M, Metzger B, Linnenbank H, Hu E L and Giessen H 2016 Nonlinear refractory plasmonics with titanium nitride nanoantennas *Nano Lett.* **16** 5708–13
- [21] George H *et al* 2019 Nonlinearities and carrier dynamics in refractory plasmonic TiN thin films *Opt. Mater. Express* **9** 3911–24
- [22] Linic S, Aslam U, Boerigter C and Morabito M 2015 Photochemical transformations on plasmonic metal nanoparticles *Nat. Mater.* **14** 567–76
- [23] Naldoni A, Shalaev V M and Brongersma M L 2017 Applying plasmonics to a sustainable future *Science* **356** 908–9
- [24] Roberts A S, Chirumamilla M, Wang D, An L, Pedersen K, Mortensen N A and Bozhevolnyi S I 2018 Ultra-thin titanium nitride films for refractory spectral selectivity [Invited] *Opt. Mater. Express* **8** 3717–28

- [25] Gargiulo J, Berté R, Li Y, Maier S A and Cortés E 2019 From optical to chemical hot spots in plasmonics *Acc. Chem. Res.* **52** 2525–35
- [26] Mayer K M and Hafner J H 2011 Localized surface plasmon resonance sensors *Chem. Rev.* **111** 3828–57
- [27] Anker J N, Hall W P, Lyandres O, Shah N C, Zhao J and Duyn R P V 2008 Biosensing with plasmonic nanosensors *Nat. Mater.* **7** 442–53
- [28] Sandtke M and Kuipers L 2007 Slow guided surface plasmons at telecom frequencies *Nat. Photon.* **1** 573–6
- [29] Noginov M A, Gu L, Livenere J, Zhu G, Pradhan A K, Mundle R, Bahoura M, Barnakov Y A and Podolskiy V A 2011 Transparent conductive oxides: plasmonic materials for telecom wavelengths *Appl. Phys. Lett.* **99** 021101
- [30] Lenci S, De Jaeger B, Carbonell L, Hu J, Mannaert G, Wellekens D, You S, Bakeroot B and Decoutere S 2013 Au-Free AlGaIn/GaN power Diode on 8-in Si substrate with gated edge termination *IEEE Electron Device Lett.* **34** 1035–7
- [31] Babicheva V E, Kinsey N, Naik G V, Ferrera M, Lavrinenko A V, Shalaev V M and Boltasseva A 2013 Towards CMOS-compatible nanophotonics: ultra-compact modulators using alternative plasmonic materials *Opt. Express* **21** 27326–37
- [32] Kim J, Naik G V, Gavrilenko A V, Dondapati K, Gavrilenko V I, Prokes S M, Glembocki O J, Shalaev V M and Boltasseva A 2013 Optical properties of gallium-doped zinc oxide—a low-loss plasmonic material: first-principles theory and experiment *Phys. Rev. X* **3** 041037
- [33] Calzolari A, Ruini A and Catellani A 2014 Transparent conductive oxides as near-IR plasmonic materials: the case of Al-doped ZnO derivatives *ACS Photon.* **1** 703–9
- [34] Kriegel I, Scotognella F and Manna L 2017 Plasmonic doped semiconductor nanocrystals: properties, fabrication, applications and perspectives *Phys. Rep.* **674** 1–52
- [35] Tegg L, Cuskelly D and Keast V J 2017 The sodium tungsten bronzes as plasmonic materials: fabrication, calculation and characterization *Mater. Res. Express* **4** 065703
- [36] Tegg L and Keast V J 2023 A review of alkali tungsten bronze nanoparticles for applications in plasmonics *Plasmonics* **18** 49–71
- [37] Blaber M G, Arnold M D and Ford M J 2010 Designing materials for plasmonic systems: the alkali–noble intermetallics *J. Phys. Condens. Matter* **22** 095501
- [38] Blaber M G, Arnold M D and Ford M J 2010 A review of the optical properties of alloys and intermetallics for plasmonics *J. Phys. Condens. Matter* **22** 143201
- [39] Dasog M 2022 Transition metal nitrides are heating up the field of plasmonics *Chem. Mater.* **34** 4249–58
- [40] Ishii S, Shinde S L and Nagao T 2019 Nonmetallic materials for plasmonic hot carrier excitation *Adv. Opt. Mater.* **7** 1800603
- [41] Guler U, Kildishev A V, Boltasseva A and Shalaev V M 2015 Plasmonics on the slope of enlightenment: the role of transition metal nitrides *Faraday Discuss.* **178** 71–86
- [42] Catellani A, D’Amico P and Calzolari A 2020 Tailoring the plasmonic properties of metals: the case of substoichiometric titanium nitride *Phys. Rev. Mater.* **4** 015201
- [43] Bannister F A 1941 Osbornite, meteoritic titanium nitride *Mineral. Mag.* **26** 36–44
- [44] Pierson H O 1966 *Handbook of Refractory Carbides and Nitrides: Properties, Characteristics, Processing and Applications* (Noyes Publications)
- [45] Sundgren J -E, Johansson B O, Rockett A, Barnett S A and Greene J E 1986 TiN_x (0.6 < x < 1.2): atomic arrangements, electronic structure and recent results on crystal growth and physical properties of epitaxial layers *AIP Conf. Proc.* **149** 95–115
- [46] Patsalas P and Logothetidis S 2001 Optical, electronic, and transport properties of nanocrystalline titanium nitride thin films *J. Appl. Phys.* **90** 4725–34
- [47] Zhang Z, Ghasemi A, Koutná N, Xu Z, Grünstäudl T, Song K, Holec D, He Y, Mayrhofer P H and Bartosik M 2021 Correlating point defects with mechanical properties in nanocrystalline TiN thin films *Mater. Des.* **207** 109844
- [48] Sundgren J-E 1985 Structure and properties of TiN coatings *Thin Solid Films* **128** 21–44
- [49] Okamoto H 2013 N–Ti (nitrogen–titanium) *J. Phase Equilib. Diffus.* **34** 151–2
- [50] Yu S, Zeng Q, Oganov A R, Frapper G and Zhang L 2015 Phase stability, chemical bonding and mechanical properties of titanium nitrides: a first-principles study *Phys. Chem. Chem. Phys.* **17** 11763–9
- [51] Yang R, Zhu C, Wei Q and Du Z 2016 Investigations on structural, elastic, thermodynamic and electronic properties of TiN, Ti₂N and Ti₃N₂ under high pressure by first-principles *J. Phys. Chem. Solids* **98** 10–9
- [52] Holmberg B 1962 Structural studies on titanium-nitrogen system *Acta Chem. Scand.* **16** 1255
- [53] Logothetidis S, Alexandrou I and Kokkou S 1996 Optimization of TiN thin film growth with in situ monitoring: the effect of bias voltage and nitrogen flow rate *Surf. Coat. Technol.* **80** 66–71
- [54] Bhadram V S, Kim D Y and Strobel T A 2016 High-pressure synthesis and characterization of incompressible titanium pernitride *Chem. Mater.* **28** 1616–20
- [55] Alfaraj N, Li K, Alawein M, Kang C H, Braic L, Zoita N C, Kiss A E, Ng T K and Ooi B S 2021 Heteroepitaxial β-Ga₂O₃ on conductive ceramic templates: toward ultrahigh gain deep-ultraviolet photodetection *Adv. Mater. Technol.* **6** 2100142
- [56] Kim J D, Kim M, Chan C, Draeger N, Coleman J J and Li X 2019 CMOS-compatible catalyst for MacEtch: titanium nitride-assisted chemical etching in vapor phase for high aspect ratio silicon nanostructures *ACS Appl. Mater. Interfaces* **11** 27371–7
- [57] Li W, Guler U, Kinsey N, Naik G V, Boltasseva A, Guan J, Shalaev V M and Kildishev A V 2014 Refractory plasmonics with titanium nitride: broadband metamaterial absorber *Adv. Mater.* **26** 7959–65
- [58] Wakabayashi H, Saito Y, Takeuchi K, Mogami T and Kunio T 2001 A dual-metal gate CMOS technology using nitrogen-concentration-controlled TiN_x film *IEEE Trans. Electron Devices* **48** 2363–9
- [59] Heavens O S 1991 *Optical Properties of Thin Solid Films* (Courier Corporation)
- [60] Tompkins H G and Hilfiker J N 2016 *Spectroscopic Ellipsometry: Practical Application to Thin Film Characterization* (Momentum Press)
- [61] Ashcroft N W and Mermin N D 1976 *Solid State Physics* (Orlando, FL: Harcourt College Publishers)
- [62] Muller R H 1969 Definitions and conventions in ellipsometry *Surf. Sci.* **16** 14–33
- [63] Wooten F 1972 *Optical Properties of Solids* (Academic)
- [64] Poelman D and Smet P F 2003 Methods for the determination of the optical constants of thin films from single transmission measurements: a critical review *J. Phys. D: Appl. Phys.* **36** 1850–7
- [65] Patsalas P, Kalfagiannis N, Kassavetis S, Abadias G, Bellas D V, Lekka C and Lidorikis E 2018 Conductive nitrides: growth principles, optical and electronic properties, and their perspectives in photonics and plasmonics *Mater. Sci. Eng. R* **123** 1–55
- [66] Fujiwara H 2018 ed R W Collins *Spectroscopic Ellipsometry for Photovoltaics: Volume 1: Fundamental Principles and Solar Cell Characterization* (Springer)

- [67] Maier S A 2007 *Plasmonics: Fundamentals and Applications* (Springer Science & Business Media)
- [68] Kreibig U and Vollmer M 1995 *Optical properties of metal clusters* vol 25 (Springer)
- [69] West P R, Ishii S, Naik G V, Emami N K, Shalaev V M and Boltasseva A 2010 Searching for better plasmonic materials *Laser Photon. Rev.* **4** 795–808
- [70] Kang J H and Kim K J 1999 Structural, optical, and electronic properties of cubic TiN_x compounds *J. Appl. Phys.* **86** 346–50
- [71] Reddy H, Guler U, Kudyshev Z, Kildishev A V, Shalaev V M and Boltasseva A 2017 Temperature-dependent optical properties of plasmonic titanium nitride thin films *ACS Photon.* **4** 1413–20
- [72] Mascaretti L, Barman T, Bricchi B R, Münz F, Li Bassi A, Kment Š and Naldoni A 2021 Controlling the plasmonic properties of titanium nitride thin films by radiofrequency substrate biasing in magnetron sputtering *Appl. Surf. Sci.* **554** 149543
- [73] Postava K, Aoyama M and Yamaguchi T 2001 Optical characterization of TiN/SiO₂(1000 nm)/Si system by spectroscopic ellipsometry and reflectometry *Appl. Surf. Sci.* **175–176** 270–5
- [74] Tripura Sundari S, Ramaseshan R, Jose F, Dash S and Tyagi A K 2014 Investigation of temperature dependent dielectric constant of a sputtered TiN thin film by spectroscopic ellipsometry *J. Appl. Phys.* **115** 033516
- [75] Judek J, Wróbel P, Michałowski P P, Oźga M, Witkowski B, Seweryn A, Struzik M, Jastrzębski C and Zborecki K 2021 Titanium nitride as a plasmonic material from near-ultraviolet to very-long-wavelength infrared range *Materials* **14** 7095
- [76] Gudmundsson J T, Brenning N, Lundin D and Helmersson U 2012 High power impulse magnetron sputtering discharge *J. Vac. Sci. Technol. A* **30** 03801
- [77] Anders A 2017 Tutorial: reactive high power impulse magnetron sputtering (R-HiPIMS) *J. Appl. Phys.* **121** 171101
- [78] Gudmundsson J T 2020 Physics and technology of magnetron sputtering discharges *Plasma Sources Sci. Technol.* **29** 113001
- [79] Ehiassarian A P, Wen J G and Petrov I 2007 Interface microstructure engineering by high power impulse magnetron sputtering for the enhancement of adhesion *J. Appl. Phys.* **101** 054301
- [80] Samuelsson M, Lundin D, Jensen J, Raadu M A, Gudmundsson J T and Helmersson U 2010 On the film density using high power impulse magnetron sputtering *Surf. Coat. Technol.* **205** 591–6
- [81] Magnus F, Ingason A S, Olafsson S and Gudmundsson J T 2012 Nucleation and resistivity of ultrathin TiN films grown by high-power impulse magnetron sputtering *IEEE Electron Device Lett.* **33** 1045–7
- [82] Lin J, Moore J J, Sproul W D, Mishra B, Rees J A, Wu Z, Chistyakov R and Abraham B 2009 Ion energy and mass distributions of the plasma during modulated pulse power magnetron sputtering *Surf. Coat. Technol.* **203** 3676–85
- [83] Brenning N, Merlino R L, Lundin D, Raadu M A and Helmersson U 2009 Faster-than-Bohm Cross-B electron transport in strongly pulsed plasmas *Phys. Rev. Lett.* **103** 225003
- [84] Patsalas P, Charitidis C, Logothetidis S, Dimitriadis C A and Valassiades O 1999 Combined electrical and mechanical properties of titanium nitride thin films as metallization materials *J. Appl. Phys.* **86** 5296–8
- [85] Haynes W M 2016 *CRC Handbook of Chemistry and Physics* (CRC Press)
- [86] Smith H A, Elhamri S, Eyink K G, Grazulis L, Hill M J, Back T C, Urbas A M, Howe B M and Reed A N 2018 Epitaxial titanium nitride on sapphire: effects of substrate temperature on microstructure and optical properties *J. Vac. Sci. Technol. A* **36** 03E107
- [87] Krekeler T *et al* 2021 Unprecedented thermal stability of plasmonic titanium nitride films up to 1400 °C *Adv. Opt. Mater.* **9** 2100323
- [88] Naik G V, Schroeder J L, Ni X, Kildishev A V, Sands T D and Boltasseva A 2012 Titanium nitride as a plasmonic material for visible and near-infrared wavelengths *Opt. Mater. Express* **2** 478–89
- [89] Gall D, Petrov I and Greene J E 2001 Epitaxial Sc_{1-x}Ti_xN(001): optical and electronic transport properties *J. Appl. Phys.* **89** 401–9
- [90] Briggs J A, Naik G V, Zhao Y, Petach T A, Sahasrabudde K, Goldhaber-Gordon D, Melosh N A and Dionne J A 2017 Temperature-dependent optical properties of titanium nitride *Appl. Phys. Lett.* **110** 101901
- [91] Barnes W L 2006 Surface plasmon–polariton length scales: a route to sub-wavelength optics *J. Opt. A: Pure Appl. Opt.* **8** S87
- [92] Reddy H, Guler U, Chaudhuri K, Dutta A, Kildishev A V, Shalaev V M and Boltasseva A 2017 Temperature-dependent optical properties of single crystalline and polycrystalline silver thin films *ACS Photon.* **4** 1083–91
- [93] Boltasseva A and Shalaev V M 2019 Transdimensional photonics *ACS Photon.* **6** 1–3
- [94] Shah D, Reddy H, Kinsey N, Shalaev V M and Boltasseva A 2017 Optical properties of plasmonic ultrathin TiN films *Adv. Opt. Mater.* **5** 1700065
- [95] Shah D, Catellani A, Reddy H, Kinsey N, Shalaev V, Boltasseva A and Calzolari A 2018 Controlling the plasmonic properties of ultrathin TiN films at the atomic level *ACS Photon.* **5** 2816–24
- [96] Shah D, Yang M, Kudyshev Z, Xu X, Shalaev V M, Bondarev I V and Boltasseva A 2022 Thickness-dependent drude plasma frequency in transdimensional plasmonic TiN *Nano Lett.* **22** 4622–9
- [97] Chawla J S, Zhang X Y and Gall D 2013 Effective electron mean free path in TiN(001) *J. Appl. Phys.* **113** 063704
- [98] Bondarev I V 2019 Finite-thickness effects in plasmonic films with periodic cylindrical anisotropy [Invited] *Opt. Mater. Express* **9** 285–94
- [99] Bondarev I V, Mousavi H and Shalaev V M 2020 Transdimensional epsilon-near-zero modes in planar plasmonic nanostructures *Phys. Rev. Res.* **2** 013070
- [100] Shah D, Kudyshev Z A, Saha S, Shalaev V M and Boltasseva A 2020 Transdimensional material platforms for tunable metasurface design *MRS Bull.* **45** 188–95
- [101] Eason R 2006 *Pulsed Laser Deposition of Thin Films: Applications-Led Growth of Functional Materials* (Wiley)
- [102] Chrisey D B H G K 1994 *Pulsed Laser Deposition of Thin Films* (Wiley)
- [103] Ashfold M N R, Claeysens F, Fuge G M and Henley S J 2004 Pulsed laser ablation and deposition of thin films *Chem. Soc. Rev.* **33** 23
- [104] Bricchi B R *et al* 2021 Optical and electronic properties of transparent conducting Ta:TiO₂ thin and ultra-thin films: the effect of doping and thickness *Mater. Adv.* **2** 7064–76
- [105] Gondoni P, Ghidelli M, Di Fonzo F, Carminati M, Russo V, Li Bassi A and Casari C S 2012 Structure-dependent optical and electrical transport properties of nanostructured Al-doped ZnO *Nanotechnology* **23** 365706
- [106] Chrisey D B, Piqué A, McGill R A, Horwitz J S, Ringeisen B R, Bubb D M and Wu P K 2003 Laser deposition of polymer and biomaterial films *Chem. Rev.* **103** 553–76
- [107] Ghidelli M, Mascaretti L, Bricchi B R, Zapelli A, Russo V, Casari C S and Li Bassi A 2018 Engineering plasmonic

- nanostructured surfaces by pulsed laser deposition *Appl. Surf. Sci.* **434** 1064–73
- [108] Sturm K, Fähler S and Krebs H-U 2000 Pulsed laser deposition of metals in low pressure inert gas *Appl. Surf. Sci.* **154–155** 462–6
- [109] Donnelly T, Krishnamurthy S, Carney K, McEvoy N and Lunney J G 2007 Pulsed laser deposition of nanoparticle films of Au *Appl. Surf. Sci.* **254** 1303–6
- [110] Casari C S and Li Bassi A 2011 Pulsed laser deposition of nanostructured oxides: from clusters to functional films *Advances in Laser and Optics Research* ed W T Arkin (UK: Nova Science Publishers, Inc) vol 72 65–100
- [111] Stafe M, Marcu A and Puscas N N 2014 *Pulsed Laser Ablation of Solids: Basics, Theory and Applications* (Springer Berlin Heidelberg) vol 53
- [112] Verhoff B, Harilal S S, Freeman J R, Diwakar P K and Hassanein A 2012 Dynamics of femto- and nanosecond laser ablation plumes investigated using optical emission spectroscopy *J. Appl. Phys.* **112** 093303
- [113] Gao B, Zhang S, Ju X, Lin Y and Wang X 2017 Femtosecond pulsed laser deposition of nanostructured TiO₂ films in atmosphere *AIP Adv.* **7** 095206
- [114] De Bonis A and Teghil R 2020 Ultra-short pulsed laser deposition of oxides, borides and carbides of transition elements *Coatings* **10** 501
- [115] Willmott P R and Huber J R 2000 Pulsed laser vaporization and deposition *Rev. Mod. Phys.* **72** 315–28
- [116] Mahjouri-Samani M *et al* 2017 Nonequilibrium synthesis of TiO₂ nanoparticle ‘building blocks’ for crystal growth by sequential attachment in pulsed laser deposition *Nano Lett.* **17** 4624–33
- [117] Divitini G *et al* 2014 Nanoscale analysis of a hierarchical hybrid solar cell in 3D *Adv. Funct. Mater.* **24** 3043–50
- [118] Rasic D, Sachan R, Chisholm M F, Prater J and Narayan J 2017 Room temperature growth of epitaxial titanium nitride films by pulsed laser deposition *Cryst. Growth Des.* **17** 6634–40
- [119] Gioti M, Arvanitidis J, Christofilos D, Chaudhuri K, Zorba T, Abadias G, Gall D, Shalaev V M, Boltasseva A and Patsalas P 2020 Plasmonic and phononic properties of epitaxial conductive transition metal nitrides *J. Opt.* **22** 084001
- [120] Saveskul N A *et al* 2019 Superconductivity behavior in epitaxial TiN films points to surface magnetic disorder *Phys. Rev. Appl.* **12** 054001
- [121] Abadias G 2008 Stress and preferred orientation in nitride-based PVD coatings *Surf. Coat. Technol.* **202** 2223–35
- [122] Huang J *et al* 2018 Nanoscale artificial plasmonic lattice in self-assembled vertically aligned nitride–metal hybrid metamaterials *Adv. Sci.* **5** 1800416
- [123] Huang J *et al* 2020 3D hybrid plasmonic framework with au nanopillars embedded in nitride multilayers integrated on Si *Adv. Mater. Interfaces* **7** 2000493
- [124] Trenczek-Zajac A, Radecka M, Zakrzewska K, Brudnik A, Kusior E, Bourgeois S, de Lucas M C M and Imhoff L 2009 Structural and electrical properties of magnetron sputtered Ti(ON) thin films: the case of TiN doped in situ with oxygen *J. Power Sources* **194** 93–103
- [125] Dhanaraj R, Mohamed S B, Kamruddin M, Kaviyarasu K and Manojkumar P A 2021 Structural properties of TiN thin films prepared by RF reactive magnetron sputtering *Mater. Today Proc.* **36** 146–9
- [126] Spengler W and Kaiser R 1976 First and second order Raman scattering in transition metal compounds *Solid State Commun.* **18** 881–4
- [127] Roy M, Sarkar K, Som J, Pfeifer M A, Craciun V, Schall J D, Aravamudan S, Wise F W and Kumar D 2023 Modulation of structural, electronic, and optical properties of titanium nitride thin films by regulated In Situ oxidation *ACS Appl. Mater. Interfaces* **15** 4733–42
- [128] Mizushiro J, Yoshimatsu K, Ohashi N, Tanaka M, Sakata O and Ohtomo A 2020 Optical and structural investigations on titanium oxynitride films for visible-UV photocatalytic applications *J. Appl. Phys.* **127** 135301
- [129] Bricchi B R, Mascaretti L, Garattoni S, Mazza M, Ghidelli M, Naldoni A and Li Bassi A 2022 Nanoporous titanium (Oxy) nitride films as broadband solar absorbers *ACS Appl. Mater. Interfaces* **14** 18453–63
- [130] Peregó A *et al* 2019 Hierarchical TiN nanostructured thin film electrode for highly stable PEM fuel cells *ACS Appl. Energy Mater.* **2** 1911–22
- [131] Trotter D M and Sievers A J 1980 Spectral selectivity of high-temperature solar absorbers *Appl. Opt.* **19** 711–28
- [132] Shan S, Chen C, Loutzenhiser P G, Ranjan D, Zhou Z and Zhang Z M 2020 Spectral emittance measurements of micro/nanostructures in energy conversion: a review *Front. Energy* **14** 482–509
- [133] Passoni L, Criante L, Fumagalli F, Scotognella F, Lanzani G and Di Fonzo F 2014 Self-assembled hierarchical nanostructures for high-efficiency porous photonic crystals *ACS Nano* **8** 12167–74
- [134] Kassavetis S, Bellas D V, Abadias G, Lidorikis E and Patsalas P 2016 Plasmonic spectral tunability of conductive ternary nitrides *Appl. Phys. Lett.* **108** 263110
- [135] Metaxa C, Kassavetis S, Pierson J F, Gall D and Patsalas P 2017 Infrared plasmonics with conductive ternary nitrides *ACS Appl. Mater. Interfaces* **9** 10825–34
- [136] Zakutayev A, Bauers S R and Lany S 2022 Experimental synthesis of theoretically predicted multivalent ternary nitride materials *Chem. Mater.* **34** 1418–38
- [137] European Commission 2020 *Critical raw materials resilience: charting a path towards greater security and sustainability COM/2020/474* <https://eur-lex.europa.eu/legal-content/EN/TXT/?uri=CELEX:52020DC0474>
- [138] Kharitonov A and Kharintsev S 2020 Tunable optical materials for multi-resonant plasmonics: from TiN to TiON [Invited] *Opt. Mater. Express* **10** 513
- [139] Patsalas P 2019 Zirconium nitride: a viable candidate for photonics and plasmonics? *Thin Solid Films* **688** 137438
- [140] Kildishev A V, Boltasseva A and Shalaev V M 2013 Planar photonics with metasurfaces *Science* **339** 1232009
- [141] Yu N and Capasso F 2014 Flat optics with designer metasurfaces *Nat. Mater.* **13** 139–50
- [142] Chirumamilla M, Chirumamilla A, Yang Y, Roberts A S, Kristensen P K, Chaudhuri K, Boltasseva A, Sutherland D S, Bozhevolnyi S I and Pedersen K 2017 Large-area ultrabroadband absorber for solar thermophotovoltaics based on 3D titanium nitride nanopillars *Adv. Opt. Mater.* **5** 1700552
- [143] Naldoni A *et al* 2020 Solar thermoplasmonic nanofurnace for high-temperature heterogeneous catalysis *Nano Lett.* **20** 3663–72
- [144] Mascaretti L, Schirato A, Fornasiero P, Boltasseva A, Shalaev V M, Alabastris A and Naldoni A 2022 Challenges and prospects of plasmonic metasurfaces for photothermal catalysis *Nanophotonics* **11** 3035–56
- [145] Cortés E, Besteiro L V, Alabastris A, Baldi A, Tagliabue G, Demetriadou A and Narang P 2020 Challenges in plasmonic catalysis *ACS Nano* **14** 16202–19